Inducing Vortices in a Bose-Einstein Condensate using light beams with orbital angular momentum

Johannes Felix Simon Brachmann

MIT-Harvard
Center for Ultra Cold Atoms
Cambridge, Massachusetts

Harvard University
Department of Physics
Cambridge, Massachusetts

Ludwig-Maximillians Universität
Fakultät für Physik
München

Inducing Vortices in a Bose-Einstein Condensate using light beams with orbital angular momentum

Diplomarbeit vorgelegt von
Johannes Felix Simon Brachmann

betreut von

Prof. Dr. Markus Greiner
Harvard University
Department of Physics
Cambridge, Massachusetts

und

Prof. Dr. Theodor Hänsch
Ludwig-Maximilians-Universität
Fakultät für Physik
München

Boston, August 2007

Erstgutachter: Prof. Dr. Theodor W. Hänsch
Zweitgutachter: Prof Dr. Stefan Kehrein

Contents

Chapter 1

Introduction

The field of ultracold atoms has experienced an increasingly rapid development in the past years. Through the development of new, more advanced experimental techniques, more and more control and knowledge about the systems under observation is gained. This allows comparison with theory to so far unreached precision.

Celebrated experimental successes of yesterday, such as the Magneto-Optical Trap [1] and the achievment of Bose-Einstein Condensation [2, 3, 4], can now be used as standard tools in a new era, making it possible to advance problems that can provide useful information for the understanding of closely related systems from other fields of physics such as solid state physics or material sciences.

The idea of quantum simulation is to study a system which is very well observable and whose parameters can be controlled in a way that it acts like another system that is experimentally difficult to access and characterize. That means, one must have the experimental techniques to be able to create a Hamiltonian for the simulation that resembles the one of the diffcult to observe system.

The idea of quantum simulation is closely related to quantum computation and goes back to an idea Richard Feynman had at the beginning of the 1980s [5, 6]: Imagine an array of atoms that we prepare in specific states 0 and 1. This is our input. Now we apply a Hamiltonian to the system that is designed specifically to perform the calculation we want to do. We let the system evolve for some time under this Hamiltonian and after a while we can look at some specific atoms in states 0 or 1 that represent the answer to our calculation. It can be shown [7] that for such a quantum computer the number of variables that must be taken into account for the simulation of a quantum system with local interactions does not increase exponentially as is the case for a classical Turing Machine. It is therefore much more efficient at simulating larger many-body systems, or stated differently, it can do it at all.

An example for a quantum simulation is the experimental realization of the Bose-Hubbard Hamiltonian in a gas of ultracold atoms using optical lattice potentials [8]. The Bose-Hubbard model was first studied for phase transitions in liquid helium and describes bosonic particles with repulsive interactions in a lattice potential. By changing the light intensity of the interfering light beams that create the optical lattice, the depth of the potential was tuned. In this way the tunneling rate of the particles to adjacent lattice sites was controlled. The phase transition from a superfluid to the Mott insulator phase occurs for a critical depth of the potential wells. In the superfluid phase, the particles are delocalized over the entire lattice. Neglecting the trapping potential for the cloud, the Mott insulator phase is characterized by the same amount of particles localized in each potential well, where the equal distribution is due to the repulsive interactions. In ultracold gases, it is also possible to tune the interactions between atoms with magnetic fields using Feshbach resonances [9]. This made it possible to tune to strong enough attractive interactions for the formation of molecules out of atom pairs [10].

Ultracold gases in optical lattice potentials are also promising for the simulation of other Hamiltonians such as those of strongly interacting many electron systems in solids, the understanding of which is important for the development of modern materials such as high temperature superconductors or novel magnetic materials. It is important to realize, that in this simulation the role of the valence electrons is taken by the atoms, whereas the optical lattice potential mimicks the periodic potential of the atom trunks. The advantage of optical lattice simulators is, that the system under observation is very clean and controllable. Also for a possible realization of a quantum computer, ultracold gases are interesting, since in no other system, states can be prepared so well and the coherence time is as long.

However, for most interesting problems today, we lack the experimental techniques to reach the regimes needed to create a Hamiltonian resembling those of the respective systems for which a simulation would be interesting or to address the system with good enough resolution.

Quantum Gas Microscope

The aim for our newly designed apparatus is to create an optical lattice simulator with high enough optical resolution to be able to address single lattice sites when the lattice spacing is small enough to allow for good tunneling rates. High resolution detection might allow a closer look at new quantum systems with new potential landscapes like Kagomé lattices [11]. It might be possible to study frustrated quantum anitferromagnetic behaviour in optical trimerized Kagomé lattices and earn more insight into systems that could not yet be accessed in condensed matter systems. Frustrated Quantum Anitferromagnets have been subject of interest in condensed matter physics for quite a while.

The high resolution of our apparatus might allow the observation of interesting dynamics and single lattice site addressability makes high resolution manipulation of the systems under observation possible. In the new scheme for inducing vortices that

is presented in this thesis, only a high enough resolution makes it possible to reach the regimes in which one fully benefits from the new approach. The high resolution projection system in our new experiment will be a big step towards projecting arbitrary potential landscapes and therefore a much more versatile tool for quantum simulations.
The use of a high numerical aperture imaging system, instead of imaging with a shorter wavelength will allow non-destructive imaging in the sense that the atoms are not lost from the lattice. Because of depth of focus, the large numerical aperture of $NA = 0.8$ restricts us to the observation of 2 dimensional systems. Figure 1.1 shows a simplified picture of the imaging setup. Both the ojective ($NA = 0.55$) and the whole imaging system (objective and hemisphere: $NA = 0.8$) are diffracion limited and, combined, have a resolution of around $0.5\mu m$. A cloud of atoms is first trapped and cooled in a different vacuum chamber in a MOT and then magnetically transported [12] into the glass cell. During evaporative cooling it is held in the glass cell by a Ioffe-Pritchard trap. After that, in some more steps, the cloud is loaded into the 2D surface trap at about $2\mu m$ distance from the plane surface of the hemisphere. This trap is created by the combined action of the magnetic trap and a blue detuned evanescent wave, which keeps the atoms away from the surface. To the surface trapping potential, an optical lattice potential will be added by two interfering laser beams which are retro reflected into themselves.

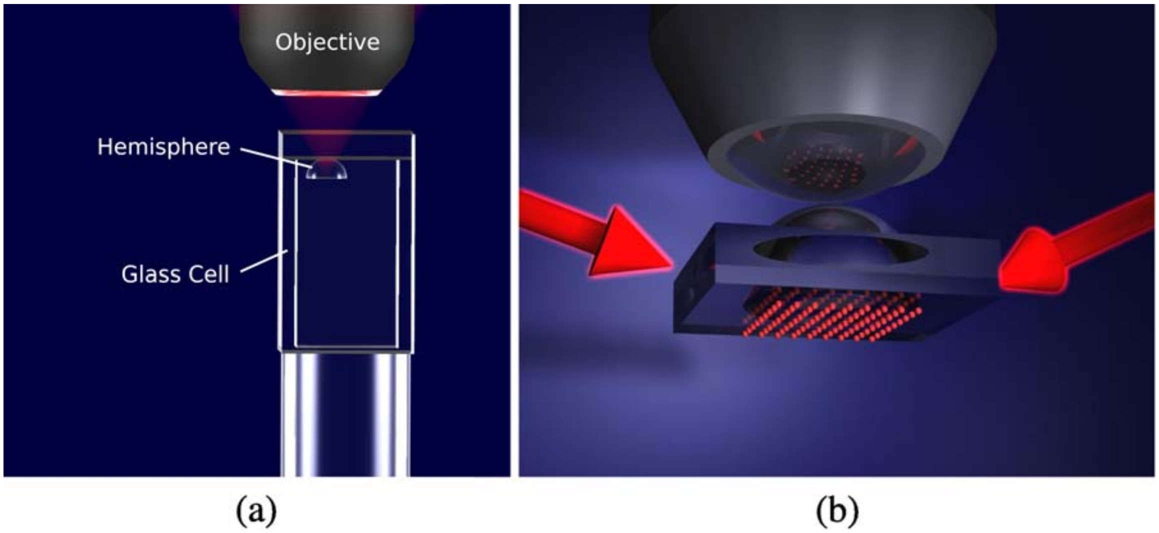

Figure 1.1: Quantum Gas Microscope. (a) the imaging system contains an objective and a hemisphere below which the atoms are held in a surface trap, (b) a 2D optical lattice is formed by two interfering laser beams below the hemisphere. I thank Jonathon Gillen (a) and Markus Greiner (b) for the pictures.

However, for the experiments presented in this thesis, neither this imaging system nor a 2D cloud are used. The temporary imaging system that was build for the experiments presented in thesis is descibed in chapter 5. The use of a 3D system makes depth of focus considerations especially important. This is treated in detail in section 3.2.4. Also, the imaging resolution is limited in the experiments to be described in chapter 6.

Vortices in Superfluids

An understanding of coherent matter waves in interacting manybody systems is important for the decription of many recently observed phenomena in atomic physics such as the observation of interference between two overlapping condensates [13], molecular condensates with bound pairs of fermions [14, 15] and quantized vortices and vortex lattices [16]. The basic ideas for this description were originally developed for superfluidity and superconductivity.

Quantized vortices in a superfluid were first observed in the "rotating bucket" experiment with liquid helium. The motion of vortex flow in superfluids is fundamentally different than classical vortex flow [17, 18]: Only above a certain rotation frequency, lines of singularity, corresponding to vortex cores form. Around these cores, there is a quantized flow of the superfluid with circulation nh/m (where n is an integer, and m the particle mass). Interestingly though, the ground state of a system with $n > 1$ angular momentum quanta for a big enough bucket (diameter >> vortex core), is not one with a single vortex of charge n, but a lattice of single charged vortices, arranging themselves in a hexagonal pattern.

In atomic physics, vortices have been used to experimentally prove that a Bose-Einstein Condensate is a superfluid. When orbital angular momentum is added to a Bose-Einstein Condensate, spontaneous formation of vortices, just like in the rotating bucket experiment, can be observed. A more detailed description of quantized vortices is given in chapter 2. There, the description is based on the assumption that the many body wavefunction is a symmetrized product of identical single particle wavefunctions (mean field).

Studying quantized vortices in atomic physics may help to develop a better understanding of superfluidity and superconductivity, since atomic physics systems are much more accessible than, for example, solid state systems. Cooper pairs of electrons in a superconductor behave like a superfluid, which can for example be seen by magnetic flux quantization (see [19], pages 256-258). When a type-II superconductor is placed in a magnetic field, screening currents are induced that prevent the field from entering the material. Since the electrons are delocalized over a large area, a quantization condition is given by the single-valuedness of the electron wavefunctions. The corresponding electron energy levels are called Landau levels. Flux can only enter the material in quantized amounts. The physics of vortices in Bose-Einstein Condensates is very similar to this, since particles are also delocalized over a large area, which leads to the same quantization condition for the atoms taking the role of electrons in a superconductor. Further the structure of vortices and dynamics of vortex creation is interesting to study and information on dissipation mechanisms and long range order can be gained from this.

Especially interesting are also vortices in quasi 2D systems as are possible to study with our Quantum Gas Microscope. With the third dimension frozen out by an external trapping potential, the transition temperature to Bose-Einstein Condensation is significantly lower by a factor of roughly $\sim \ln N$ than the temperature at which the thermal wavelength is comparable to the particle spacing. But independent from that, a transition to a superfluid phase takes place [20]. For a 2D system, below this critical temperature T_c, the Berezinskii-Kosterlitz-Thouless theory predicts a phase transition that is associated with the behaviour of vortices and has recently been observed [21]: Below T_c vortices are only found in bound pairs of vortices of different circulation direction, while above T_c unbound vortices proliferate. The holographic technique to stimulate vortices, which is presented in this thesis should make it possible to directly create these vortex pairs, the excitation of which is usually thermaly driven.

An interesting 2D effect to simulate would be the Quantum Hall Effect. The techniques presented in this thesis might help to achieve that. The Quantum Hall Effect has been observed at low temperatures (samples cooled with liquid helium $\Rightarrow$ electron wavefunctions delocalized) in boundary layers between semiconductors with a different bandgap. Since the Fermi energy must be the same in both materials when they are contacted, the conduction band gets deformed and a 2 dimensional electron gas (2DEG) forms in the contact region. When a strong enough magnetic field is applied (for small fields the system behaves classical: Hall Effect), the electron energy is quantized in Landau levels, which can be seen by the same reasoning as given for flux quantization earlier. However, since the 2DEG is restricted to the area of the probe, another conditon arises: Not all classical particle trajectories are allowed, but only ones with certain diameters and origins. For magnetic field strengths, for which not all particles can be put in Landau levels, there is another possibility however: The surplus particles can be in so called "edge states" close to the physical boundaries of the sample. Particles in these states on one side of the probe all move in the same direction which gives rise to the vanishing electrical resistance of the probe. The band structure, Hall- and longitudinal voltages for the integer Quantum Hall Effect are shown in figure 1.2. For the Fractional Quantum Hall Effect, particle interactions need to be included. These lead to the formation of quasiparticles with less than unit charge.

To simulate the quantum hall effect in atomic physics one would need to stimulate vortices in a cloud of atoms in superfluid phase and enter the regime corresponding to

high magnetic field shown in figure 1.2, where the electrons are mostly in the lowest Laudau state, which, in the atomic physics system, corresponds to a situation where the number of vortices is comparable to the number of atoms in the cloud.
Three regimes of vortex states can be characterized by filling factors of the number of particles N_p to the number of vortices N_v: In the high filling factor regime (see [22, 23]), where all experiments so far were situated, the ground state for a trap that confines the cloud to a region much larger than the healing length ξ^3, is given by single charged vortices which assemble themselves in a hexagonal lattice. In the second regime with filling factors $N_p/N_v \approx 10$, the elastic shear strength of the vortex lattice is predicted to drop low enough for quantum fluctuations to melt the lattice, and strongly correlated boson liquid states which resemble those in the fermionic Fractional Quantum Hall effect should be observable. In the third regime, characterized by filling factors $N_p/N_v < 10$, quasiparticle excitations obeying fractional statistics are predicted [24]. A decrease of the lattice elastic shear strength was observed in the $N_p/N_v \approx 500$ regime [25].

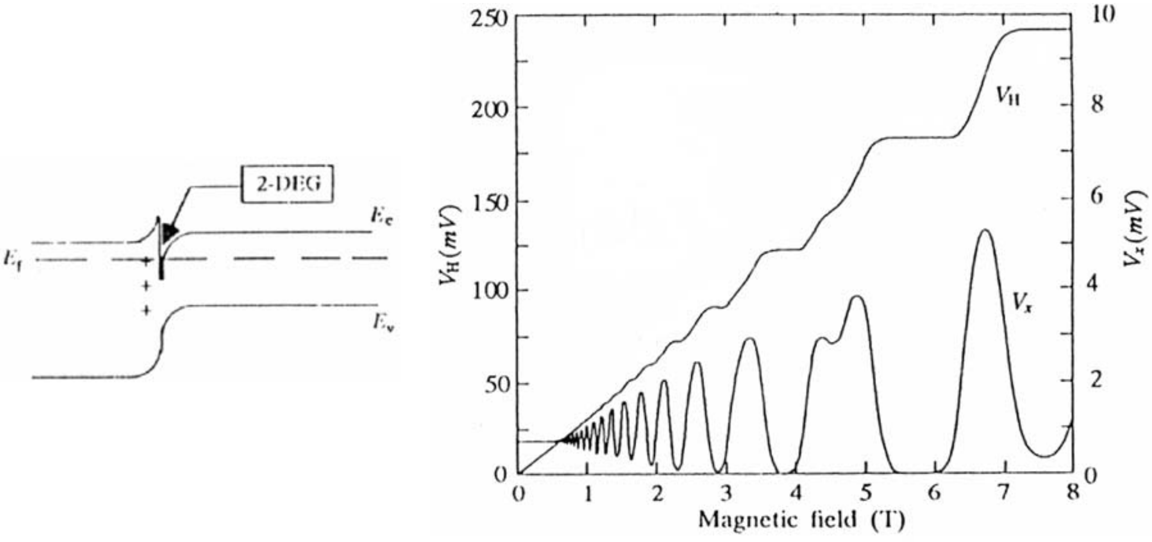

(a) (b)

Figure 1.2: Integer Quantum Hall Effect. Taken from a figure in [26]. (a) a 2 dimensinal electron gas forms at the border of a AlGaAs/GaAs heterostructure, (b) Hall (V_H) and longitudinal (V_x) voltages as a function of the magnetic field strength

Holographic technique to induce vortices in a Bose-Einstein Condensate

The most common, current technique to induce vortices in Bose-Einstein Condensates is to somehow create an anisotropy in the trap used to capture the atom cloud, which can then be moved around to transfer angular momentum to the cloud. The trap anisotropy is usually created by either changing the magnetic field that traps the atoms and having it rotate, or, more commonly, by moving the focus of a detuned laser beam around in the cloud and thus adding an AC-Starkshift potential to the trapping potential. The fastest rotation reached so far was done in two steps: First, the cloud was set into slow rotation using a magnetic stirrer. Then, an evaporative spinup technique [27], which removed atoms that carried less than average angular momentum, was used. This was done by a radio frequency field propagating along the axes of rotation. With the combined use of magnetic stirring and evaporative spinup the Boulder group [25] reached the lowest Landau level regime, spinning up the condensates to 99% of the trap frequency and reaching filling factors $N_p/N_v \approx 500$.

In this thesis, a new, more versatile technique to induce vortices in a gas of ultracold atoms is presented. By coherent transfer of momentum from a light beam carrying orbital angular momentum to atoms in an ultracold gas cloud, vortex states can be directly excited. In this way, arbitrary vortex pattern with arbitrary circulation direction and charge (number of angular momentum quanta contained in the vortex) can be created. Since these are not ground states of the system, interesting dynamics might be observed and maybe information about systems gained, that can currently not be generated in stationary state. Holograms are, in principle, capable of creating any wanted wavefront (in paraxial approximation) of the electro magnetic field. The holographic technique to produce light beams with orbital angular momentum, discussed in chapter 3, makes it possible to create a wide range of different light beams with different momentum states to be transferred. This is clearly an advantage over other methods in which angular momentum is added to the whole cloud and stationary state vortices form spontaneously.

Several problems make it hard to reach the regime of low filling factors in steady state. The radius of the depleted area close to the vortex center (vortex core), where propability density of particles is very low, is on the order of the healing length (see section 2.3.1) of the gas and proportional to the inverse square root of the density times the scattering length. This makes it hard to fit many vortices into a typical cloud of a diameter of $30\mu m$. Also, for a harmonic confining potential, the trap is only capable of holding a cloud with a rotation frequency that is lower than the trap frequency. This means that, when a cloud is set into fast rotation, the density and the healing length will chage by a significant amount, until ultimately the trapping force does not exceed the centrifugal force. This is unlike the behaviour of an electron gas in a solid, which is strongly bound to the solid.

The high resolution of our Quantum Gas Microscope might allow us to reach the low

filling factor regime below $N_p/N_v = 10$ in a non equilibrium situation when combined with the holographic technique to produce orbital angular momentum light beams. Since we can load about one atom per lattice site in our 2D trap and are able to address them individually, this allows us to transfer one quantum of angular momentum to each of the atoms if a corresponding hologram is used. We hope to find interesting physics even in the non equilibrium situation created this way.
The results in chapter 6 show the first vortices made in our group, in this new way. It can be seen that a high resolution projection optics is essential for vortex creation in this way as it was the limiting factor in the described experiments.

Raman transitions

As explained before, a coherent process of angular momentum transfer is needed to induce vortices. To achieve this, a Raman laser setup was built in the course of the work for this Diploma thesis. With the setup, transitions between the hyperfine ground states and/or the magnetic sublevels and/or momentum states of Rubidium 87 can be driven via the D1 line. For the two coherent light fields needed for Raman transitions, the light of a single $795nm$ laser diode is split up. One of the light beams then passes through a hologram, creating a spatial phase of the light field that carries angular momentum. The difference in frequency needed for transitions changing the hyperfine state is obtained from an electro optical modulator. For fast switching and transitions between Zeeman states an acousto optical modulator is used. The Raman setup is described in detail in chapter 4.

Optical Lattices from Holograms

Another interesting use of the holographic technique presented in this thesis is to make a hologram that creates an optical lattice. For this, the object beam and the conjugate beam can be interfered (see chapter 3.2, [28]). Loosing most of the light to the zeroth order can be avoided by the use of a phase mask (see section 3.2.3). The advantage of using a hologram to create an optical lattice is that it is possible to use a laser with a short coherence length which does not need to be frequency stabilized extremely well. This is because object and conjugate beam are created from the same beam and are consequently coherent with respect to each other. Also very convenient is, that the wavelength of the lattice laser can be changed without changing the lattice spacing. That means the detuning can also be used to change the trap depth, affecting spontaneous emission rates. Also it is possible to use a laser with a very broad frequency spectrum, as has, for example, a pulsed laser.
Other than by inducing vortices it is also possible to mimick a magnetic field for neutral particles with a rotating optical lattice [29]. Since it might be possible to rotate a hologram using an ultra vibration free motor with an air bearing, as are

available today, this approach is also promising.

Chapter 2

Bose-Einstein Condensates

The phenomenon of Bose-Einstein Condensation is very fundamental in the sense that it is only due to the counting statistics of Bosons. No particle interactions of any special kind need to be considered in a description of it. That means it can be predicted in a theory of ideal particles with fixed particle number, as was done by Albert Einstein in 1924 [30]. About 70 years later, Bose-Einstein Condensation was first realized in an atomic physics system [2, 3, 4]. Today, creating a Bose-Einstein Condensate is almost a standard procedure, making this macroscopic quantum object available as a tool for fundamental research.

After a short review of Bose-Einstein Condensation in an ideal gas, parameters of a Bose-Einstein Condensate of interacting atoms are calculated using mean field theory. The Gross-Pitaevskii equation will be presented in a short manner and used to calculate some parameters of the condensate in the Thomas-Fermi approximation. Also for the description of quantized vortex states in a Bose-Einstein Condensate the Gross-Pitaevskii equation will be used. Even though interactions are not necessary for a description of Bose-Einstein Condensation, they are needed for a Bose-Einstein Condensate to become a superfluid [19], which is the interesting property for vortex experiments.

2.1 Bose-Einstein Condensation of an ideal gas

From the grand partition function, the average occupation numbers $\langle n_{\mathbf{p}} \rangle$ of a state with momentum $\mathbf{p}$

$$\langle n_{\mathbf{p}} \rangle = \frac{z e^{-\beta \epsilon_{\mathbf{p}}}}{1 - z e^{-\beta \epsilon_{\mathbf{p}}}} \tag{2.1}$$

and the equation of state of the ideal Bose gas can be obtained (for detailed description of this section, see [19]):

$$\frac{P}{k_BT} = -\frac{4\pi}{h^3}\int_0^\infty dp\, p^2 \log(1 - ze^{-\beta p^2/2m}) - \frac{1}{V}\log(1-z) \tag{2.2}$$

$$\frac{1}{v} = \frac{4\pi}{h^3}\int_0^\infty dp\, p^2 \frac{1}{z^{-1}e^{\beta p^2/2m} - 1} + \frac{1}{V}\frac{z}{1-z} \tag{2.3}$$

where P is the pressure, T the temperature, V the volume, $z = exp(\mu/k_BT) = exp(\beta\mu)$ the fugacity and v the volume per particle. The integrals are carried out over the momentum p and are obtained by replacing sums in the limit $V \to \infty$. Since they diverge for $z \to 1$ and $\mathbf{p} = 0$, these single terms have been split off. This divergence is connected to Bose-Einstein Condensation.

Expressing the equation of state using the functions $g_{5/2}(z)$ and $g_{3/2}(z)$ (see [19]), equation 2.3 can be used to derive the occupance of the lowest ($\mathbf{p} = 0$) level at low temperatures:

$$\frac{\langle n_{\mathbf{p}=0}\rangle}{N} = \begin{cases} 0 & \left(\frac{\lambda^3}{v} \leq g_{3/2}(1)\right) \\ 1 - \left(\frac{T}{T_c}\right)^{3/2} & \left(\frac{\lambda^3}{v} \geq g_{3/2}(1)\right) \end{cases} \tag{2.4}$$

Here, $\lambda = (2\pi\hbar^2)/(mk_BT)^{1/2}$ is the thermal wavelength, which is, at T_c, comparable to the interparticle spacing. $g_{3/2}(1) = 2.612\ldots$ and the critical temperature T_c is defined as

$$T_c = \frac{2\pi\hbar^2}{(vg_{3/2}(1))^{2/3}mk_B} \tag{2.5}$$

Equantion 2.4 describes the phenomenon of Bose-Einstein Condensation: Below the critical temperature T_c, a finite fraction of the particles can be found in the same ($\mathbf{p} = 0$) state. For $T \lesssim T_c$ only a small fraction of the particles is found in the condensed phase; as T is lowered, more and more particles are in the ground state, until at $T = 0$ finally, $\langle n_{\mathbf{p}=0}\rangle/N = 1$.

The condensed phase of an ideal gas has inifinite compressibility, which is, of course unphysical for gases in atomic physics. Furthermore, superfluidity, which is the most important property for the work in this thesis, is not found in this idealized system [19].

This is due to the equation of state used here. To obtain the integrals in 2.2 and 2.3, the limit of an infinite system with $V \to \infty$ has been considered. Thus, the energy spectrum is continuous. The *Landau criterion* for superfluidity is, that a body moving through a superfluid must have a critical velocity in order to excite higher energy levels in the fluid and loose energy through that. This critical velocity depends on the energy gap between ground state and excited levels and is thus zero for a continuous energy spectrum.

2.2 The Gross-Pitaevskii Equation

For ultracold atoms, scattering processes are of very low energy. In a mean field description of the condensed phase including interactions, it is therefore sufficient to consider zero energy scattering. The Lippmann-Schwinger equation for the scattering matrix T in momentum space

$$T(\mathbf{k}', \mathbf{k}; E) = U(\mathbf{k}', \mathbf{k}) + \frac{1}{V} \sum_{\mathbf{k}''} \frac{U(\mathbf{k}', \mathbf{k}'')}{E - \frac{\hbar^2 k''^2}{m} + i\delta} T(\mathbf{k}'', \mathbf{k}'; E) \tag{2.6}$$

contains a sum over intermediate momentum states $\mathbf{k}''$ [1]. An effective interaction $\tilde{U}(\mathbf{k}', \mathbf{k}; E)$ can be introduced by splitting this sum into two groups. In one part $\mathbf{k}''$ vectors corresponding to an energy higher than $e_c = \hbar^2 k_c^2/2m$ are summed up. This contribution is regarded as the effective potential $\tilde{U}$ which takes the place of U in the Lippmann-Schwinger equation 2.6, now containing a sum over the remaining momentum states. For ultracold atoms, choosing a cut-off energy $e_c = 0$, is enough to describe the scattered wavefunction on the physically relevant length scale intermediant between interparticle spacing and cloud size of a typical Bose-Einstein Condensate well. Doing this the scattering matrix T reduces to the effective interaction U_0, which is related to the scattering length a by

$$U_0 = \frac{4\pi\hbar^2}{m} a \tag{2.7}$$

U_0 is independent of the specific shape of the interaction potential and the momentum of the particles. In position space, the interaction is a point interaction $U_0\delta(\mathbf{r} - \mathbf{r}')$.

In a Hartree description of the ground state, it is assumed, that the many body wavefunction Ψ for N particles is a symmetrized product of single particle wavefunctions ϕ:

$$\Psi(\mathbf{r}_1, \mathbf{r}_2, \ldots, \mathbf{r}_N) = \prod_{i=1}^{N} \phi(\mathbf{r}_i) \tag{2.8}$$

The Hamiltonian contains the kinetic energy, the external potential and the effective point interaction potential:

$$H = \sum_i \Big(\frac{\mathbf{p}_i^2}{2m} + V(\mathbf{r}_i) \Big) + U_0 \sum_{i<j} \delta(\mathbf{r} - \mathbf{r}') \tag{2.9}$$

Neglecting terms of order $1/N$, the time independent Gross-Pitaevskii equation can be be obtained from the expectation value of the energy:

$$E = \int d\mathbf{r} \left(\frac{\hbar^2}{2m} |\nabla\psi(\mathbf{r})|^2 + V\psi(\mathbf{r})|^2 + \frac{1}{2} U_0 \psi(\mathbf{r})|^4 \right) \tag{2.10}$$

---

[1] For all derivations in this section, see [31]

Minimizing the energy under the condition that the total number of particles is constant, leads to the time independent Gross-Pitaevskii equation:

$$-\frac{\hbar^2}{2m}\nabla^2\psi(\mathbf{r}) + V(\mathbf{r})\psi(\mathbf{r}) + U_0|\psi(\mathbf{r})|^2\psi(\mathbf{r}) = \mu\psi(\mathbf{r}) \tag{2.11}$$

Here μ is a Lagrange multiplier, which can be identified as the chemical potential. The function ψ is the single particle wavefunction in the approximation where terms of order $1/N$ are neglected. Equation 2.11 has the form of a Schrödinger equation with an external potential V, in which the nonlinear term $U_0|\psi(\mathbf{r})|^2$ takes the mean field interactions with the other Bosons into account.
To treat dynamical problems, as the free expansion of an interacting condensate in time of flight, the Gross-Pitaevskii equation 2.11 can be generalized to same type of time dependent Schrödinger equation,

$$-\frac{\hbar^2}{2m}\nabla^2\psi(\mathbf{r}) + V(\mathbf{r})\psi(\mathbf{r}) + U_0|\psi(\mathbf{r})|^2\psi(\mathbf{r}) = i\hbar\frac{\partial\psi(\mathbf{r})}{\partial t} \tag{2.12}$$

the consistency of which with equation 2.11 can be shown [31].
We come to the conclusion that in an interacting Bose-Einstein Condensate, the system can be well described with the assumption that all particles are in the same state $|\psi\rangle$. It is an eigenstate of a Schrödinger-type equation in which the interaction potential between atoms enters as a nonlinearity. These interactions are sufficiently described by a constant, which measures their strength, and the momentum of the colliding particles does not need to be taken into account.

2.2.1 Radius of a condensed cloud

In the Thomas-Fermi approximation, the kinetic energy term of the Gross-Pitaevskii equation 2.11 is neglected. Except at the boundries of the cloud, this is a good approximation for large atom numbers, where the interaction energy outbalances the kinetic energy. Thus the single particle probability density can be found as

$$n(\mathbf{r}) = |\psi(\mathbf{r})|^2 = \frac{\mu - V(\mathbf{r})}{U_0} \tag{2.13}$$

where μ is the chemical potential. The boundary of the cloud is determined by $\mu = V(\mathbf{r})$. Taking the external trapping potential $V(\mathbf{r}) = 1/2m\omega_0^2\mathbf{r}^2$ to be harmonic and isotropic, we arrive at an expression for the radial extension of the cloud

$$R_0 = (15Na)^{1/5}\Big(\frac{\hbar}{m\omega_0}\Big)^{2/5} \tag{2.14}$$

Equation 2.12 can be used to calculate the free expansion of the cloud in time of flight. With a variational method using a Gaussian trial function

$$\psi(r,t) = \frac{A\sqrt{N}}{R^{3/2}} e^{i\beta m r^2/2\hbar} e^{-r^2/2R^2} \tag{2.15}$$

and minimizing the energy of the state, an approximation using the asymptotic behaviour can be found as

$$R(t) = \sqrt{\frac{2}{3}\omega_0^2 t^2 R^2(0) + R^2(0)} \tag{2.16}$$

In this trial function, β and R are the parameters used to miminize the energy; A is a constant.

2.3 Rotating Condensates

The motion of superfluids is much more restricted than classical fluid flow, since, nonrelativistically, the velocity is propotional to the gradient of the phase ς of the wavefunction

$$\mathbf{v} = \frac{\hbar}{m}\nabla\varsigma \tag{2.17}$$

where m is the mass of a single particle with wavefunction ϕ. Since $\nabla \times \mathbf{v} = 0$, the motion of the fluid is irrotational, unless there exists a phase singularity. In the mean field description of a Bose-Einstein Condensate using the Gross-Pitaevskii equation 2.11, particles are delocalized over the entire cloud, which gives rise to the quantization condition for Landau levels. The single-valuedness of the wavefunction restricts the change of phase around a closed contour containing a phase singularity to be a multiple of 2π

$$\Delta\varsigma = 2\pi l \tag{2.18}$$

where the integer l is the is the number of orbital angular momentum quanta (charge) per particle, contained in the vortex. Thus the circulation Γ around the closed contour is quantized

$$\Gamma = \oint \mathbf{v} \cdot d\mathbf{s} = l\frac{h}{m} \tag{2.19}$$

and the single particle wavefunction must vary as $e^{il\varphi}$, where φ is the azimuthal angle. The velocity of a purely azimuthal flow with an axis of symmetry perpendicular to the vortex flow can then be computed as

$$v_\varphi = \frac{lh}{2\pi m\rho} \tag{2.20}$$

where ρ is the distance from the vortex core which is also distance from the center of the trap. The superfluid vortex motion is thus very different from the motion of a vortex in a classical fluid where there is friction between different "shells" at distances ρ from the vortex core: The phase of the particle wavefunctions varies fast close to the core and slow far from the core, as is required by angular momentum conservation.

The results presented in section 2.3.1 show, that the lowest energy state of a not too tightly confined cloud, in a harmonic trap containing l quanta of angular momentum has l vortex cores, instead of vortices with higher charge. Figure 2.1(b) shows a lattice of n single charged vortices that have arranged themselves in their equilibrium configuration, equally spaced in a hexagonal pattern, which respresents the ground state of the system with $n = l$ angular momentum quanta per particle. This absorption image was taken after $41.5ms$ of time of flight (see [32]), so that the Condensate cloud and the vortex cores, which can clearly be seen as dark regions, have expanded. Angular momentum was added to the cloud by use of the stirring

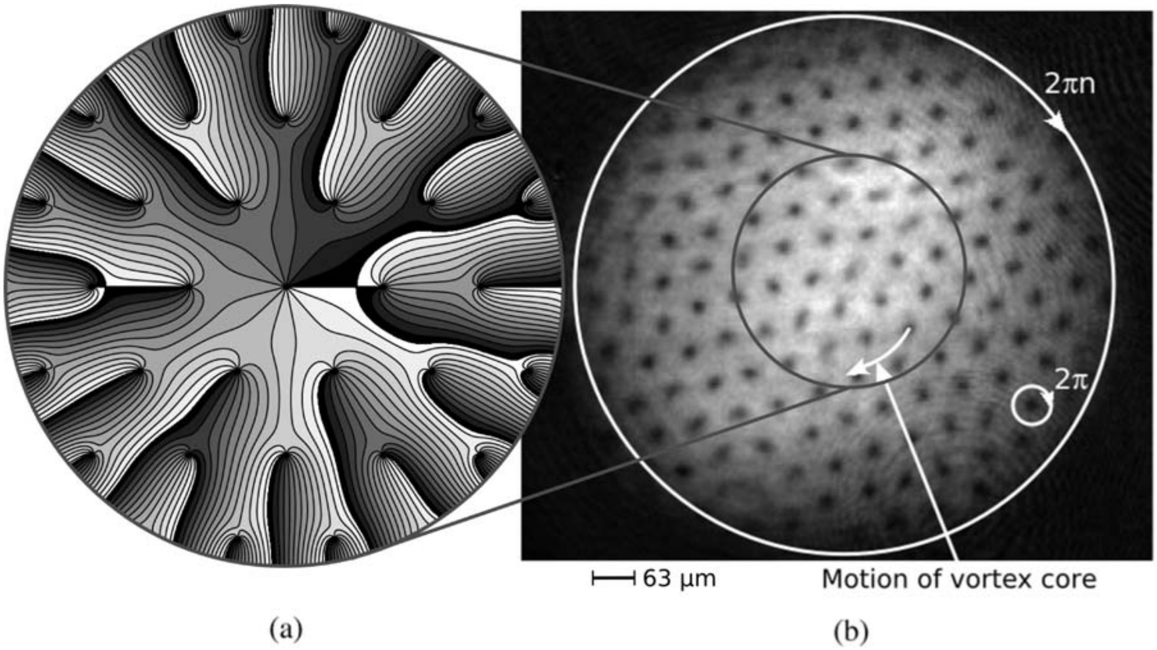

(a) (b)

Figure 2.1: (a) calculated phase pattern for the region of the cloud marked by the grey cirlce. Shading represents phase. Clearly, the interference of all phases of the single charged vortices can be seen. (b) vortex lattice. Phase variances along 2 paths are indicated by circles and arrows. Off centered vortices are moving around the center. The absorption image is taken from [32], a publication by C. Raman, J. R. Abo-Shaeer, J. M. Vogels, K. Xu and W. Ketterle

technique described earlier, so that all the vortices have the same circulation direction. Arrows in the picture indicate the behaviour of the phase of the wavefunction, which varies as $e^{i\varphi}$ around every single vortex, and as $e^{in\varphi}$ around the whole cloud containing n vortices, where again φ is the azimuthal angle in cylindrical coordinates. Due to the presence of the other vortices, off-centered vortices move around the center vortex. This corresponds to Kelvins theorem in classical hydrodynamics, that states, that the circulation around a contour moving with the fluid is a constant in time (for rotation frequencies see [31]). Quantum mechanically the movement can be seen from equation 2.17 by calculating the phase pattern of the condensate wavefunction for the vortex lattice, which has been done in an image plane crossection through the cloud and is shown in Figure 2.1(a).

In the new phase imprinting technique presented in this thesis, the phase of a light field is imprinted on a cloud of atoms. Thus this phase pattern of the atomic wavefunctions resembles the phase of the classical eletromagnetic field in a beam crossection. Pictures and a description of the intensity and the phase of the light beam that has passed through hologram creating the shown phase pattern are shown in chapter 3. The matter wave character of the atom cloud is shown in a nice way by this correspondence.

2.3.1 Some Vortex Parameters

In this section, the results from a calculation of some experimentally relevant parameters of rotating condensates are presented. For example, the density function of a rotating condensate close to the vortex core, and its development in time of flight are interesting for the observation of vortex states. When setting up an absorption imaging system, one needs to be sure that, with the chosen resolution, it is possible to see the core after a given time of flight.

The energy of the vortex and the extension of the vortex core in equilibrium can be calculated from equations 2.10 and 2.11. In the wave function, we make use of the known phase variance of a single vortex:

$$\psi(\mathbf{r}) = f(\rho, z)e^{il\varphi} \tag{2.21}$$

where f is a real function giving the modulus of the amplitue. In cylindrical coordinates the energy functional 2.10 and the Gross-Pitaevskii equation 2.11 for this wavefunction become

$$E = \int d\mathbf{r} \left[\frac{\hbar^2}{2m}\left(\left(\frac{\partial f}{\partial \rho}\right)^2 + \left(\frac{\partial f}{\partial z}\right)^2\right) + \frac{\hbar^2 l^2}{2m}\frac{f^2}{\rho^2} + V(\rho, z)f^2 + \frac{U_0}{2}f^4\right] \tag{2.22}$$

and

$$-\frac{\hbar^2}{2m}\left(\frac{1}{\rho}\frac{d}{d\rho}\left(\rho\frac{df}{d\rho}\right) + \frac{d^2 f}{dz^2}\right) + \frac{\hbar^2}{2m\rho^2}l^2 f + V(\rho, z)f + U_0 f^3 = \mu f. \tag{2.23}$$

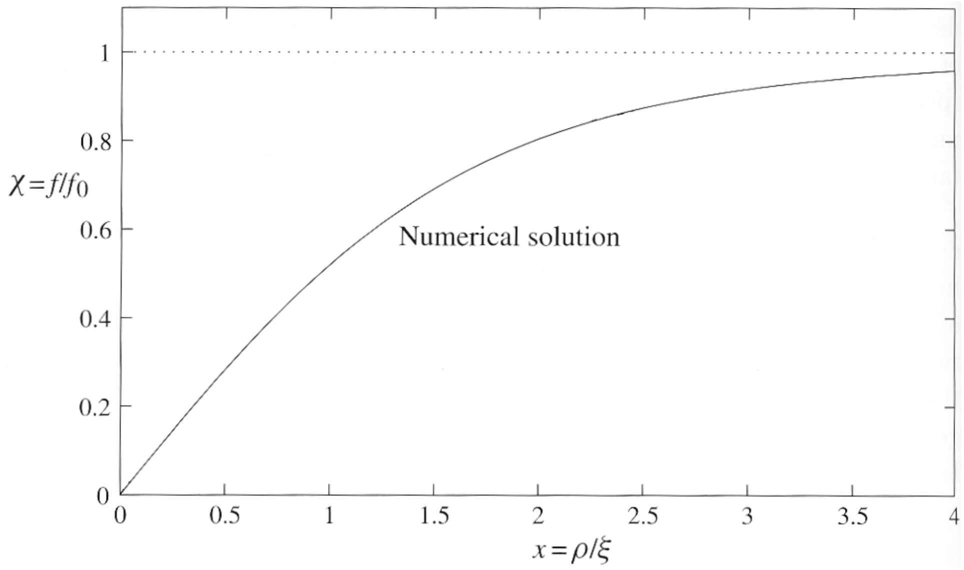

Figure 2.2: Equilibrium size of a vortex core. The graph is taken from [31]. The in trap healing length of our ^{87}Rb condensate is approximately $1\mu m$

Single vortex in an infinite medium without potential

A numerical solution of the Gross-Pitaevskii equation 2.23 for the idealized case of a $l = 1$ single charged vortex in an infinite medium with uniform potential $V = 0$ in is shown in Figure 2.2. In this graph, the distance x from the vortex center has been scaled in units of the healing length $\xi = \sqrt{(8\pi m)/(hnU_0)}$ of the condensate wavefunction and f is shown in units of the value $f_0 = f(\rho \to \infty)$ of f far from the vortex core. In the expression for the healing length, m is again the mass of the particles, n the density and U_0 the effective potential. From the numerical solution for f, the energy associated with the vortex can be computed using equation 2.22. Since this relation diverges for $\rho \to \infty$, the integral is only carried out over a finite distance $0 \ldots b$, where we assume $b >> \xi$. Numerical integration gives

$$\epsilon_v = \frac{\pi n \hbar^2}{m} \ln \left(1.464 \frac{b}{\xi} \right). \tag{2.24}$$

Higher charged vortices and vortex interaction

Equation 2.22 can be used to calculate the energy of higher charged vortices. To see, if the ground state of a system with $l > 1$ angular momentum quanta is given by a single multiply charged vortex or l single charged ones, interactions between vortices must be considered. In [31] it is shown, that the interaction energy between two vortices is to logarithmic accuaracy

$$\epsilon_{int} = \frac{2\pi l_1 l_2 n\hbar^2}{m} \ln\left(\frac{R}{d}\right). \tag{2.25}$$

if we assume the cloud radius R to be much bigger than d, the distance between vortex cores, and this distance $d >> \xi$. A calculation of the numerical factor in equation 2.22 confirms that the energy of a multiply charged vortex is higher, than the one for two interacting vortices with lower charge. This is true for trapping functions is monotonously increasing and that satisfy the given condition for the radius.

An equilibrium vortex in a cloud trapped by an harmonical potential

More relevant for experiment is the energy of a vortex in a cloud trapped by a harmonical potential. For stirring experiments, the critical velocity of stirring, at which it is favorable for a vortex to enter the cloud can be gained from this.
Assumed is a cloud that can be described well with the Thomas-Fermi approximation ($\xi << R$), with the Thomas-Fermi radius R. The energy of a vortex in a 3D harmonical trap can be calculated using 2.22 close to the vortex core ($\xi << \rho_1 << R$) and integrating up the kinetic energy of the particles far from the core ($\rho_1 << \rho << R$), taking the density function into account (see [33]). The density profile in the direction along the vortex line of singularity (z-axes) is taken into account by integrating slices of the cloud, perpendicluar to the z-axes. The energy of a single vortex is thus found to be

$$E = \frac{4\pi n(0)\hbar^2}{3m} Z \ln\left(0.671\frac{R}{\xi_0}\right) \tag{2.26}$$

where Z is the semi axes of the cloud in the z-direction and ξ_0 is the healing length at the center of the cloud in absence of rotation.
From this the angular momentum of the cloud and the critical angular velocity for stirring can be calculated.

$$\Omega_c = 2\frac{\hbar}{mR^2} \ln\frac{0.888R}{\xi_0} \tag{2.27}$$

Since the behaviour of the cloud is treated to be the same for small ρ as for the case without potential, the healing length and the size of the vortex core are approximately the same.

Time of flight expansion of a vortex core

Since vortex core sizes are of the order of the healing length $\xi \approx 1\mu m$ and Thomas-Fermi radii are usually about 15 - 20μm, observation is much easier if the cloud is expanded in time of flight. The approch to calculate the behaviour of a vortex core in time of flight is similar to the one mentioned in 2.2.1, only that the trial function now takes the phase $e^{il\varphi}$ into account. Figure 2.3 is a graph from [34] where the expansion of a vortex core is calculated in this manner.

Two regions can be distingushed in this graph: For small values, the vortex core size almost immidiately takes on the value given by the healing length through the density. The vortex core grows more rapidly than the cloud itself. In the second region when interactions play a negligible role, the core expands as the cloud does, which is basically given by free particle movement. Figure 2.3 confirms, that vortex cores are more easily seen in a weak coupling regime.

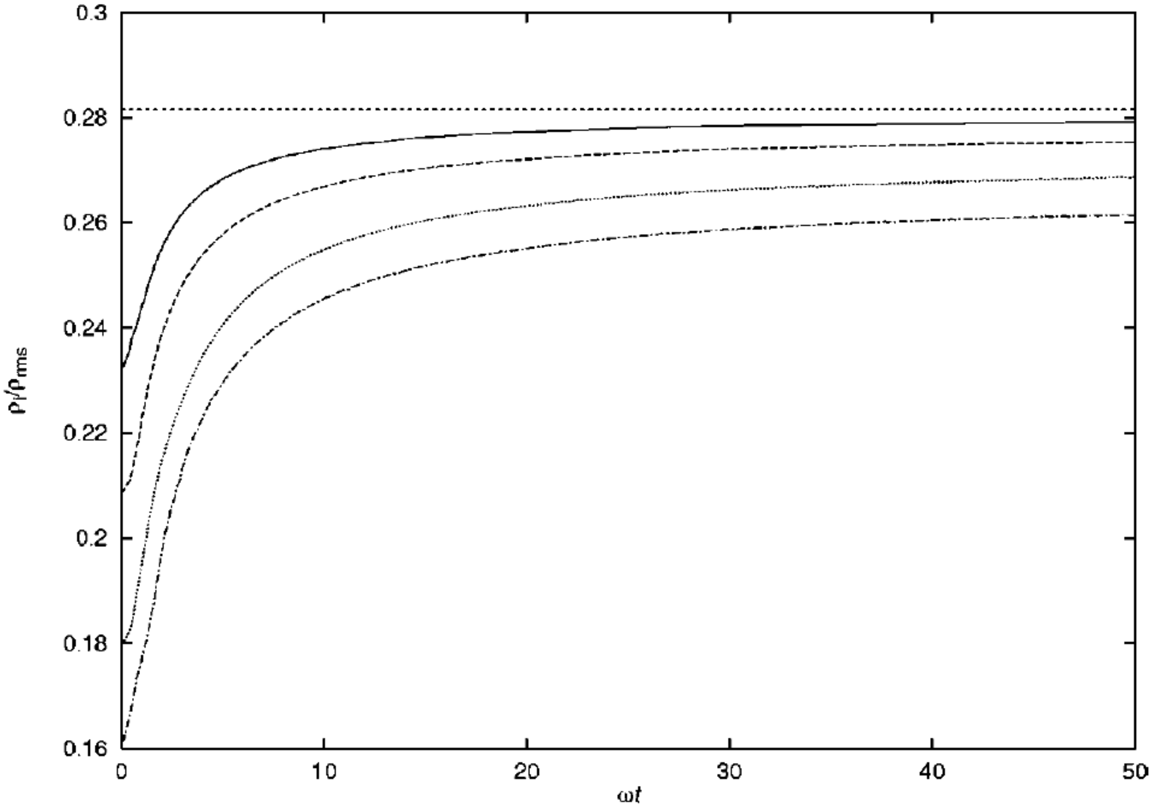

Figure 2.3: Expansion of the vortex core size compared to the cloud size as a function of the product between trap frequency and time. ρ_i is the radius where the density of particles reaches the value $1/e$. Curves are for Na/a_{osc} = 10 (full line), 10 (dashed line), 20 (dotted line) and 30 (dot-dashed line). The horizontal line shows the value for the free particle limit with $Na/a_{osc} = 0$.

Chapter 3

Light beams with orbital angular momentum

After a short excursion on Laguerre-Gaussian modes, this chapter will describe the holograms used to create light beams with orbital angular momentum. The use of holograms is shown to be very versatile, since a wide variety of vortex states can easily be produced, including states with vortex patterns or high orbital angular momentum states. Besides, holograms of good quality as described here, are interesting for many other applications, including new ways to create optical lattices.

3.1 Laguerre-Gaussian beams as an example for beams with orbital angular momentum

The angular momentum of a classical electromagnetic field can be separated into a spin part and a part corresponding to orbital angular momentum. However it has generally been assumed that this separation is unphysical for the following reasons. Firstly, in its rest frame, the spin part should correspond to the total angular momentum of the particle. But this rest frame does not exist for a photon. Secondly, the action of the associated quantum mechanical operators for spin and orbital angular momentum parts are believed to yield unphysical states, when appiled on a physical state of the radiation field. Rather recent investigation shows however that both parts are separately measurable quantities, but the associated quantum mechanical operators are not angular momentum operators [35]. For example it can be shown that all the components of the associated spin operator commute, so it does not generate rotations of the polarization field.

For linearly polarized light, the vector potential of a Laguerre Gaussian mode in

Lorentz gauge can be written as [36]

$$\mathbf{A} = u(r,\phi,z)e^{-ikz}\hat{x} \tag{3.1}$$

with:

$$\begin{aligned} u_{pl}(r,\phi,z) = {} & \frac{C}{\sqrt{1+\frac{z^2}{z_R^2}}}\left(\frac{r\sqrt{2}}{w(z)}\right)^l L_p^l\left(\frac{2r^2}{w^2(z)}\right)e^{-r^2/w^2(z)} \\ \times \ & e^{ikr^2z/(2(z^2+z_R^2))}e^{-il\phi}e^{i(2p+l+1)tan^{-1}(z/z_R)} \end{aligned} \tag{3.2}$$

where cylindrical coordinates have been chosen. L_p^l are the Laguerre polynomials with l specifying the charge, or number of orbital angular momentum quanta per photon, of the vortex state. $w(z)$ is the well known function describing the spread of a gaussian beam with Rayleigh length z_R. The function $u(r,\phi,z)$ satisfies the paraxial wave equation. A phase variation of $e^{-il\phi}$ is characteristic for beams with orbital angular momentum. $e^{-il\phi}$, being the Eigenfunction of the orbital angular momentum operator, describes a state with orbital angular momentum.
Following [36] and using equation 3.1, the momentum density per unit power of the Laguerre Gaussian field mode is found to be:

$$\wp = \frac{1}{c}\left[\frac{rz}{z^2+z_R^2} \mid u\mid^2 \hat{r} + \frac{l}{kr} \mid u\mid^2 \hat{\phi} + \mid u\mid^2 \hat{z}\right] \tag{3.3}$$

where $\hat{r}$, $\hat{\phi}$ and $\hat{z}$ are corresponding unit vectors in cylindrical coordinates. The contributions correspond to the beamspread ($\hat{r}$), orbital angular momentum ($\hat{\phi}$) and linear momentum ($\hat{z}$). Figure 3.1 shows the Poynting vector $c^2\wp$, which describes a spiral along the direction of propagation.
It is the $\hat{\phi}$ component of the total angular momentum that is coherently transferred

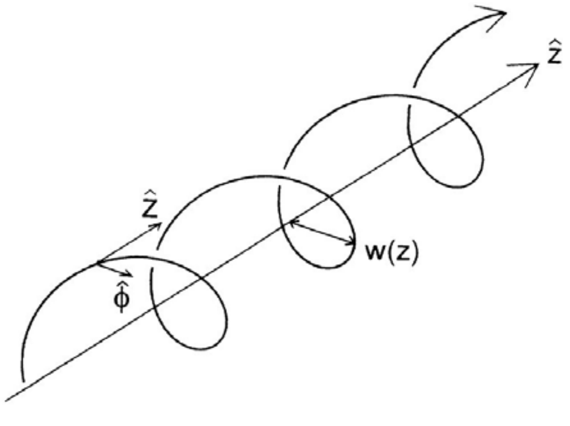

Figure 3.1: Poynting vector of a linearly polarized Laguerre-Gaussian mode. This figure is taken from [36]

to the atoms of a Bose-Einstein Condensate to induce a vortex state.
However, Laguerre Gaussian modes are not a very good choice to induce vortex states in a cloud of ultracold atoms. This is due to the rather large area in the beam crossection in which the intensity of the beam is small and therefore the interaction of the atoms with the light field does not induce many atoms in that region to populate the vortex state. For our purposes, a light beam approximating a constant intensity over the whole area of the beam as good as possible is desirable.
In figure 3.2 the intensity and phase of a L_0^1 beam is shown. For this mode the intensity for small r is proportional to $1/r$ as can be seen from equation 3.1.

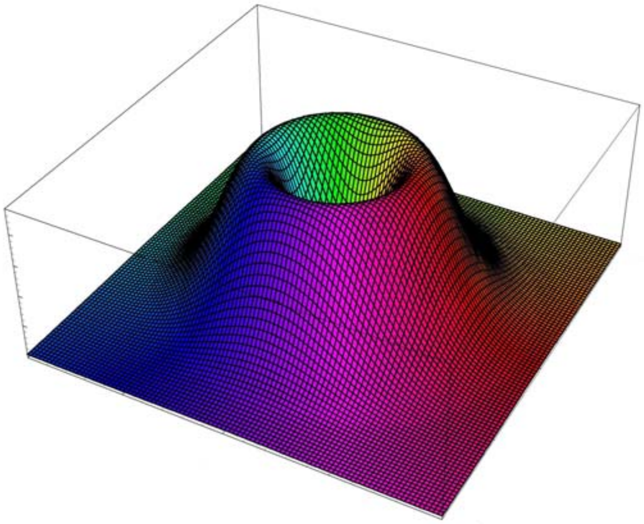

Figure 3.2: L_0^1 beam. A cross section in the x-y plane. Coloring represents phase, height beam intensity.

3.2 Holograms to produce light beams with orbital angular momentum

Besides a short introductory description of holography, this section describes the holograms used in our experiment and how to make them. For good image quality the resolution and evenness of the hologram features is crucial. It will be shown that binary holograms provide a good approximation to a greyscale hologram for our purposes and can be manufactured with high precision.

3.2.1 Holography

The idea of holography is, to create an image that not only contains the intensity information, but also the information about phase. Consider a light beam that propagates in the positive z-direction. The field amplitudes in every plane $(x,\ y, z = z_0)$ perpendicular to the propagation direction at some time t_0 contain all information about the field amplitudes of *the same* wavefront at all times t in all planes (x, y, z). In paraxial approximation a hologram reproduces the field amplitude of the original beam with which it was recorded and thereby recreates a 3 dimensional image of an object.
Figure 3.3 [1] shows how a hologram is taken:
A coherent beam of light is split up; one part illuminates an object, the other is used as a reference beam. In some plane $z = z_0$ the light field scattered off the object spacially overlaps with the reference beam and forms an interference pattern. The interference pattern is stationary since both light fields are coherent, and can be recorded onto a photographic film.

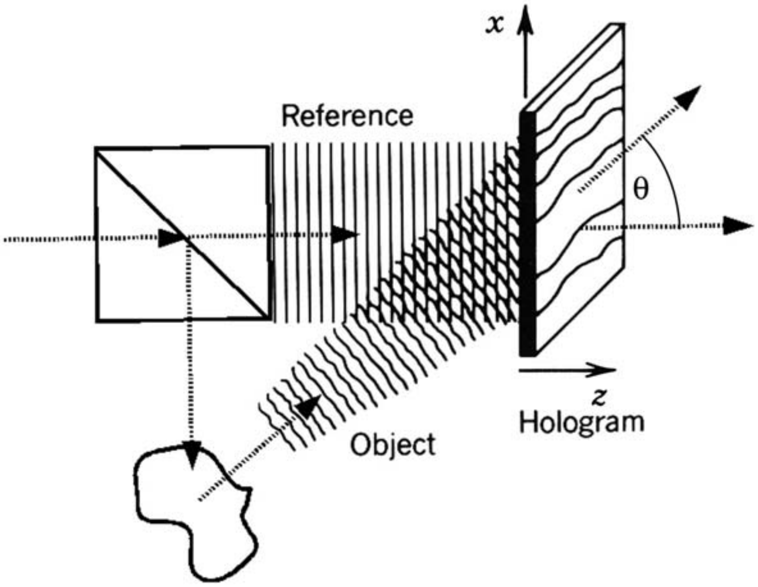

Figure 3.3: Recording of a hologram

If the processed hologram is again placed in the reference light field, it acts as a mask: The reference light can only pass through the hologram where there was constructive interference when it was recorded. Under the original angle of incidence θ between object and reference beam (see Figure 3.3), the light fields passing through

---

[1] Part of this Figure is taken from [28]

the mask have the phases needed to again form the original object beam. However it needs to be mentioned, that the object beam is not the only beam created when projecting a hologram (see section 3.2.2).

A good reference on holography can be found in [28], or for a more detailed explanation [37].

3.2.2 Calculation of holograms

The information on holography can now be used to calculate the hologram for a light beam with orbital angular momentum. Looking again at Figure 3.3 we take the object beam as the beam carrying orbital angular momentum and calculate the interference with the reference beam in the plane z_0.

Consider first the simple case of a hologram for a light beam containing a single vortex with charge l. Since, as mentioned in section 3.1, a constant intensity over the whole size of the vortex is desirable, we take the object beam be

$$A_{obj}(\mathbf{x}) = e^{il\phi(\mathbf{x})}e^{i\mathbf{k}_{obj}\mathbf{x}} \tag{3.4}$$

which is a plane wave multiplied by the characteristic classical phase of a light field with a single vortex that carries l quanta of orbital angular momentum per photon. $\phi(\mathbf{x})$ is the function that returns the angle ϕ in plane $z = z_0$ (see Figure 3.4), which we take as the reference plane to define the absolute phase. Choosing the intensity as constant will produce a physical light beam in which the size of the region with small intensity close to the phase singularity at the center of the vortex is determined by the projection optics.

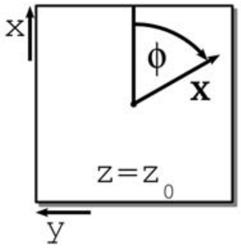

Figure 3.4: Looking into the $-z$-direction. $\phi(\mathbf{x})$ returns the angle ϕ in the plane $z = z_0$

As the reference beam, we take a plane wave:

$$A_{ref}(\mathbf{x}) = e^{i\mathbf{k}_{ref}\mathbf{x}} \tag{3.5}$$

To calculate the interference pattern we add the amplitudes 3.4 and 3.5 and take the modulus squared:

$$I(\mathbf{x}) = \mid e^{i\mathbf{k}_{ref}\mathbf{x}} + e^{il\phi(\mathbf{x})}e^{i\mathbf{k}_{obj}\mathbf{x}} \mid^2 = 2(1 + \cos(\mathbf{k}_{ref}\mathbf{x} - (\mathbf{k}_{obj}\mathbf{x} + l\phi(\mathbf{x})))) \tag{3.6}$$

For calculating the hologram we choose the plane $z_0 = 0$. Again, θ specifies the angle between the plane wave reference beam and the plane wave component of the object beam. Further,

$$|\mathbf{k}| = |\mathbf{k}_{ref}| = |\mathbf{k}_{obj}| = \frac{2\pi}{\lambda} \tag{3.7}$$

With these definitions, we get for the interference pattern in the plane of the hologram:

$$I(\mathbf{x}_{|z=0}) = 2(1 + \cos(|\mathbf{k}|\sin(\theta)x + l\phi(\mathbf{x}_{|z=0}))) \tag{3.8}$$

where x is a cartesian coordinate. A microscopy image of a binary approximation to this intensity pattern is shown in figure 3.7, section 3.2.3.

Multiple vortex holograms

It is now easy to calculate holograms for light beams with multiple vortices at arbitrary positions, rotation direction and charges reaching from one to very high numbers:

- The rotation direction of a vortex is given by the sign in the exponent of the $exp(\pm l\phi)$ multiplicant. Looking in the propagation direction of the beam, "+" creates clockwise rotation, "−" rotates counterclockwise.
- l specifies the charge.
- By adding arbitrary vectors $\mathbf{a}_n$ to the argument of the function $\phi(\mathbf{x} - \mathbf{a}_n)$, vortices can be positioned.

As an example, the following expression for an object beam describes a light beam with four vortices of charges $l = 1, 2, 4, 8$, positioned at locations $\mathbf{a}_1 \ldots \mathbf{a}_4$. The vortices with charges $l = 1, 2$ are rotating counterclockwise; those with charges $l = 4, 8$ are rotating clockwise. Figure 3.5 shows a phase plot in a cross section of this object beam.

$$A_{obj}(\mathbf{x}) = e^{-i\phi(\mathbf{x}-\mathbf{a}_1)}e^{-i2\phi(\mathbf{x}-\mathbf{a}_2)}e^{i4\phi(\mathbf{x}-\mathbf{a}_3)}e^{i8\phi(\mathbf{x}-\mathbf{a}_4)}e^{i\mathbf{k}_{obj}\mathbf{x}} \tag{3.9}$$

Choosing again 3.5 as a reference beam, the intensity pattern in the plane $z_0 = 0$ of the hologram is found to be:

$$\begin{aligned} I(\mathbf{x}_{|z=0}) &= 2[1 + \cos(|\mathbf{k}|\sin(\Theta)x - \phi((\mathbf{x}-\mathbf{a}_1)_{|z=0})) - 2\phi((\mathbf{x}-\mathbf{a}_2)_{|z=0})) + \\ &\quad + 4\phi((\mathbf{x}-\mathbf{a}_3)_{|z=0})) + 8\phi((\mathbf{x}-\mathbf{a}_4)_{|z=0}))] \end{aligned} \tag{3.10}$$

Figure 3.6 shows the intensity pattern described by equation 3.10. On first sight, the basic structure of the intensity pattern (or hologram) is a stripe pattern, like a diffraction grating. This is due to the plane wave components in the object and

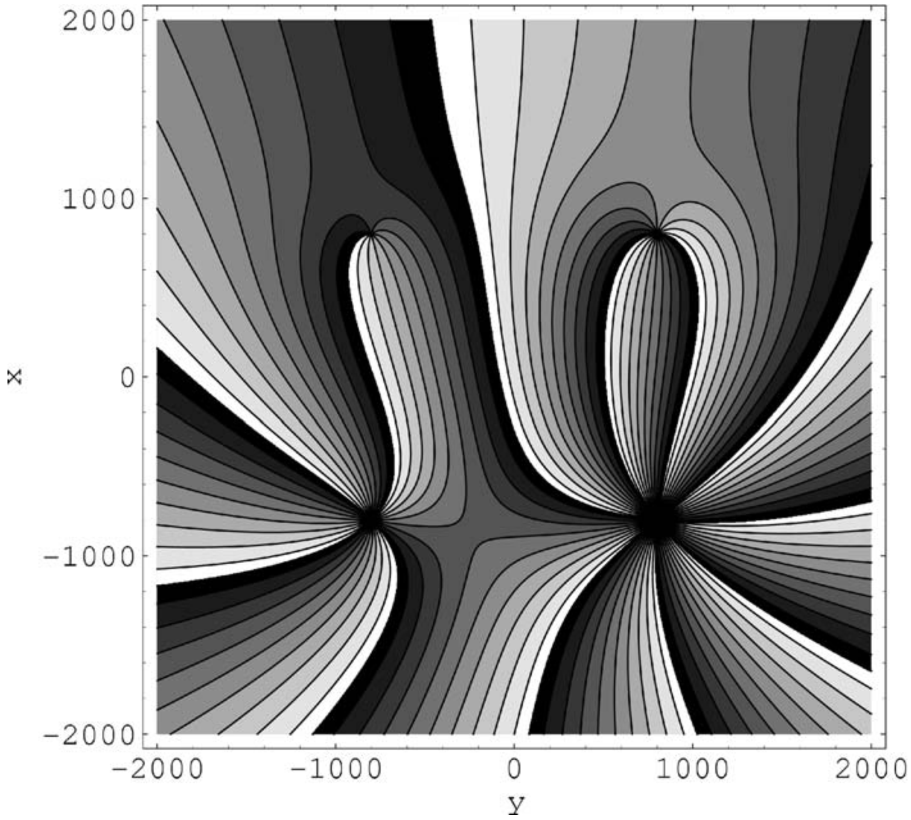

Figure 3.5: Phase plot in a cross section of the object beam 3.9. Coloring represents phase.

reference beams. Two coherent plane waves with propagation directions different by the angle θ will create an intensity pattern $1 + \cos(|\mathbf{k}| \sin(\theta) x)$ which looks like a greyscale diffraction grating. This immidiately gives a hint what beams other than the object beam we can expect to be created when projecting the hologram: A sinusoidal diffraction grating will, of course, produce three diffraction orders!

The fork-like structures are creating the vortices. A more intuitive explanation on how this happens will be given in section 3.2.3. In this example, vectors $\mathbf{a}_1 ... \mathbf{a}_4$ were chosen to position the vortex centers on the corners of a square. In the beam, each vortex core is positioned at the center of the respective fork structure, where the upper row contains the counter clockwise rotating vortices with charges $l = 1$ (left) and $l = 2$ (right); the $l = 4$ (left) and $l = 8$ (right) charged clockwise rotating vortices are in the lower row.

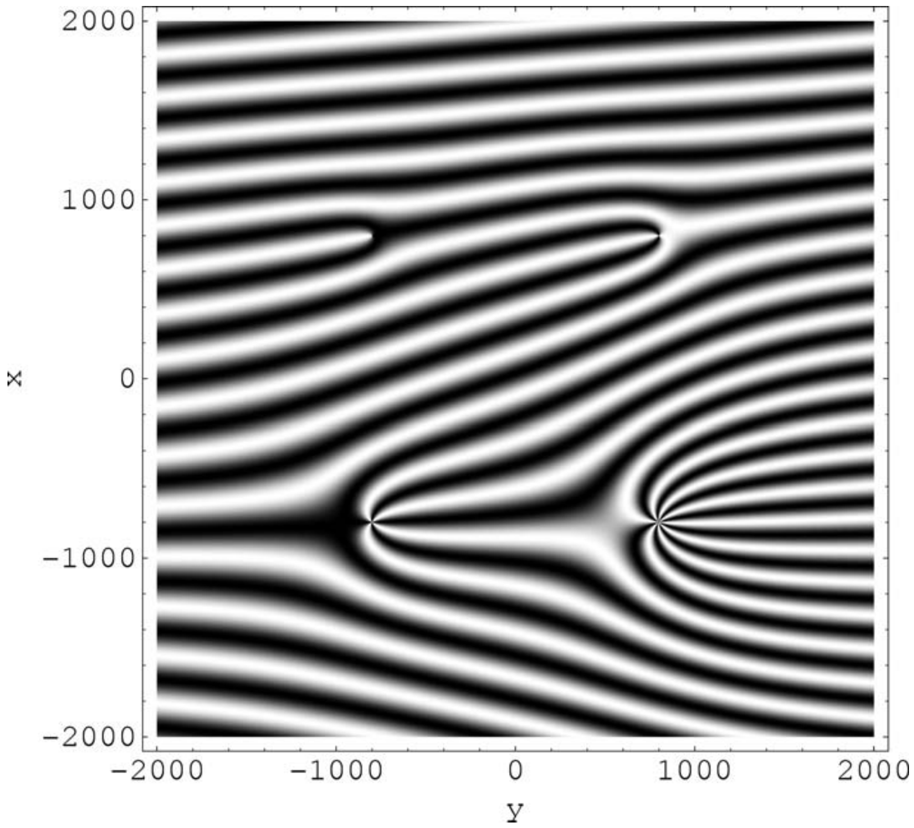

Figure 3.6: Hologram for a beam with 4 vortices of charge $l = 1, 2, 4, 8$. The upper and lower row vortices have opposite directions.

3.2.3 Binary Holograms

Now that we know how to calculate the hologram for our specific application, we need a way to produce holograms in good quality. Obviously a good resolution, on the order of the projection light wavelength, of the hologram features, is needed to achieve that. Also, since we are considering thin holograms and try to create a mask that blocks the reference light in a plane, the material used needs to extinct the light well or needs to create a well defined phaseshift of the reference beam (see the following paragraph on phase holograms).

Glass substrates with good surface quality are, of course, widely available, which suggests that a chrome mask might be the right choice for a hologram. Chrome masks can be produced in very good resolution with standard lithographic techniques, but are usually "binary", which means they cannot represent greyscale, but are either opaque or transparent. To convert a hologram to a binary approximation, we only need to define a threshold for the intensity in the corresponding equation and specify for which values the hologram is transparent and for which the light gets blocked.

For the specific holograms we are interested in, it is not so much of an obstacle that no greyscale can be represented. The resulting changes in the light fields when the greyscale hologram is changed to a binary hologram, can be seen from a Fourier analysis of the pattern. A sinusoidal pattern contains only one spatial frequency (or positve and negative of this frequency and a constant). This means that the Fourier transform of the light field that is passing through the hologram will only contain the $\pm 1st$ and $0th$ orders. The binary pattern with its sharp edges, on the other hand contains many different spatial frequencies. These will show up as higher orders in the Fourier transform of the light field passing through the hologram. How many higher orders there are depends on the line spacing and width. This determines the angle at which the orders are diffracted, which can't be larger than 90°. This is equivalent to the statement that structures smaller than the wavelength of the light can't be resolved by it. Since we are only using one of the first orders anyway, the only difference to the sinusoidal pattern will be the efficiency of how much of the incoming light is diffracted into the first orders.

Figure 3.7 shows two microscopy pictures of a chrome mask for a single vortex described by equation 3.8. Looking at the one with larger magnification, it can be seen that the resolution of the laser lithograph used is indeed good: All the lines are smooth and the fork structure is nicely displayed.

As before, the hologram mostly looks like a diffraction grating, so the reference beam, after the hologram gets split up into diffraction orders. The first diffraction order propagates at an angle at which the light passing through one slit is 2π out of phase relative to the light passing through the next slit. To see how the phaseshift $e^{il\phi}$ is created in the beam, consider a path around the fork structure as drawn in the picture. On the left side of the fork structure the difference of the phases passing through the upper and lower slits is roughly 2π in the first diffraction orders. Following the path on the right side however, 2 slits are passed, amounting to a phaseshift of 4π. That means 2π of phase are gained in the first diffraction orders moving around the path. By the same reasoning it is easy to see how all diffraction orders behave: The mth diffraction order has a phaseshift of $2\pi m$ around a path as shown in figure 3.7. Further, two respective orders with same m are rotating in opposite directions.

Phase mask holograms

The use of a chrome mask as a hologram wastes most of the light, which might be a downside for many applications. First a hologram like the one shown in figure 3.7 reflects half the light from the chrome coated regions. Then usually only the first diffraction order(s) are used, which leaves most of the light, that is contained in the zeroth order, unused. For inducing vortices in a ^{87}Rb Bose-Einstein Condensate, this is not of importance however, since very little light, on the order of $10\mu W/mm^2$, is needed for the Raman transitions, even for relatively large detunings of up to $5GHz$

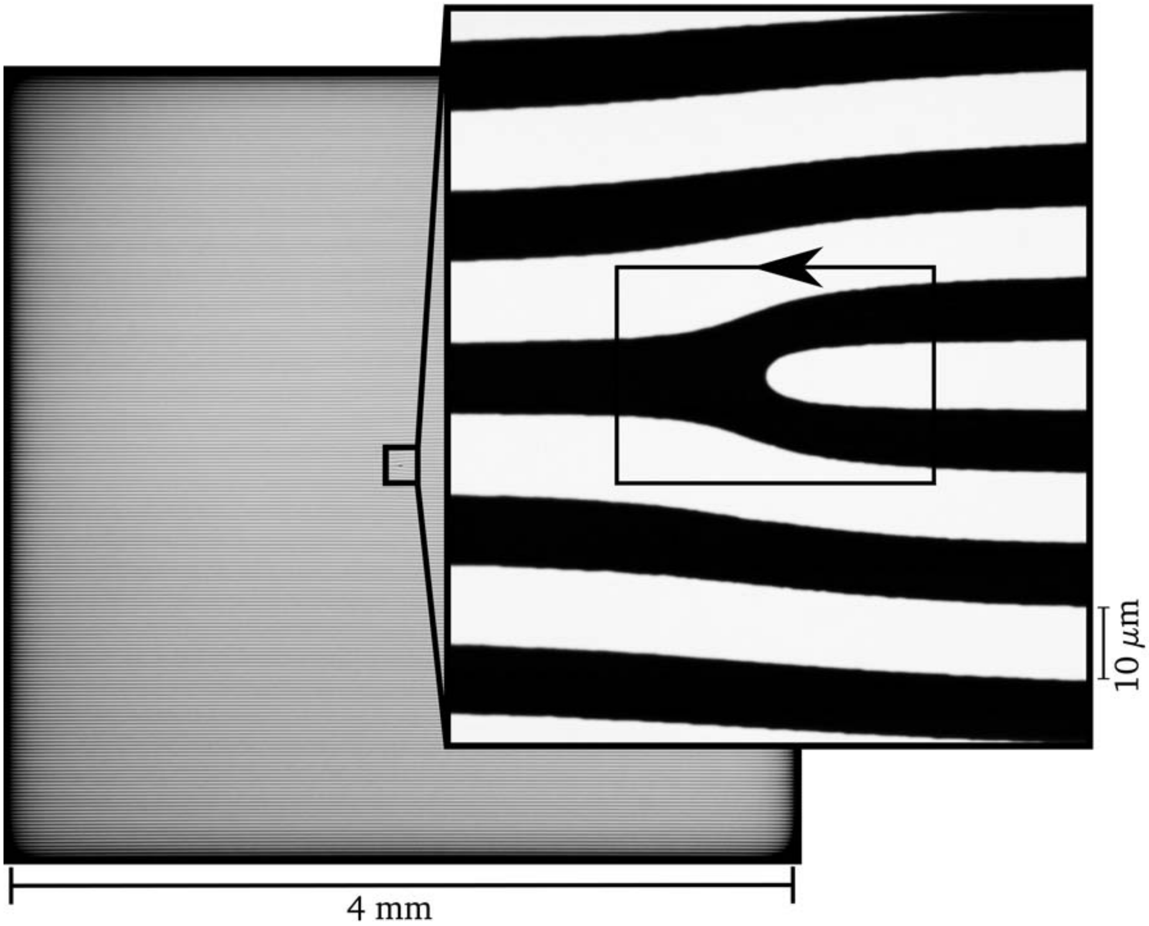

Figure 3.7: Microscopy images of a binary hologram for a single vortex state.

(see chapter 4). This is due to the small saturation intensity for transitions between the lowest fine structure levels of ^{87}Rb. For other applications where high intensity is needed, as for example creating an optical lattice by interfering the first orders of a hologram, this needs to be avoided.

A way to get more intensity into the interesting orders is to use a phase mask as shown in figure 3.8. Instead of blocking the light, a microstructured coating is applied on a substrate. At regions where the light gets blocked in a chrome mask, the light travelling into the z-direction now experiences a well defined phase shift of π at regions with coating as compared to regions without coating in figure 3.8. By the reasoning used for figure 3.7 in the preceding paragraph, it is easy to see that the 0th order, containing most of the light for a chrome mask hologram, gets suppressed when a phase mask is used. The light passing through the uncoated regions interferes destructivly with the light passing through the coated regions. The first order, how-

ever, contains most of the light suppressed from the 0th order, since in regions where there would have been destructive interference in a recording process as described figure 3.3, now the object beam gets an extra π of phase, changing from destructive to constructive interference. This also means that a phase hologram, so to speak, uses the positive and negative of a hologram at the same time.
To calculate how much more efficient a phase mask compared to the mask that blocks the light is, Fourier analysis can be used again. Neglecting the fork structures for the vortices, but only comparing simple diffraction gratings, the pattern of the chrome mask can be one dimensionally represented by same length intervals of amplitude 1 and 0 along an x-dimension. By Fourier transformation of this function, it can be found that around 10% of the light that hits the hologram gets diffracted into one first order. For the phase mask the amplitude is taken to be 1 and -1 in the respective intervalls. By the following argument it can be seen that for the phase mask, around 40% of the light intensity are diffracted into one first order. The phase mask pattern can be changed to the chrome mask pattern by a shift $y = (x + 1)/2$. In the Fourier transformation, this gives a delta distribution for the constant term, while the amplitude for the other points is half as big. Thus, since the intensity is the square of the amplitude, four times more light is in one first order, when a phase mask is used.

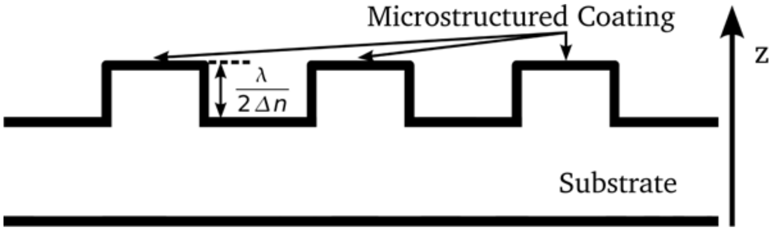

Figure 3.8: Phase mask hologram. The height of the structure induces a phase shift of $\lambda/2$ compared to air or other surrounding media.

Critical for phase masks is a substrate of low surface roughness and even thickness over the whole beam area. The coating thickness must, of course, be defined well below wavelength. Microstructured coatings with this high of a precision can be manufactured using a lithograpic technique combined with liftoff.

3.2.4 Hologram Projection

To use a hologram it needs to be projected onto an image plane. Figure 3.9 (a) shows the intensity of the first order beam of the hologram shown in figure 3.7 in the image plane over a section in which the intensity of the gaussian beam used to project the hologram is approximately constant. The region of small intensity at the center of the vortex can clearly be seen. As mentioned before, its size is determined by the

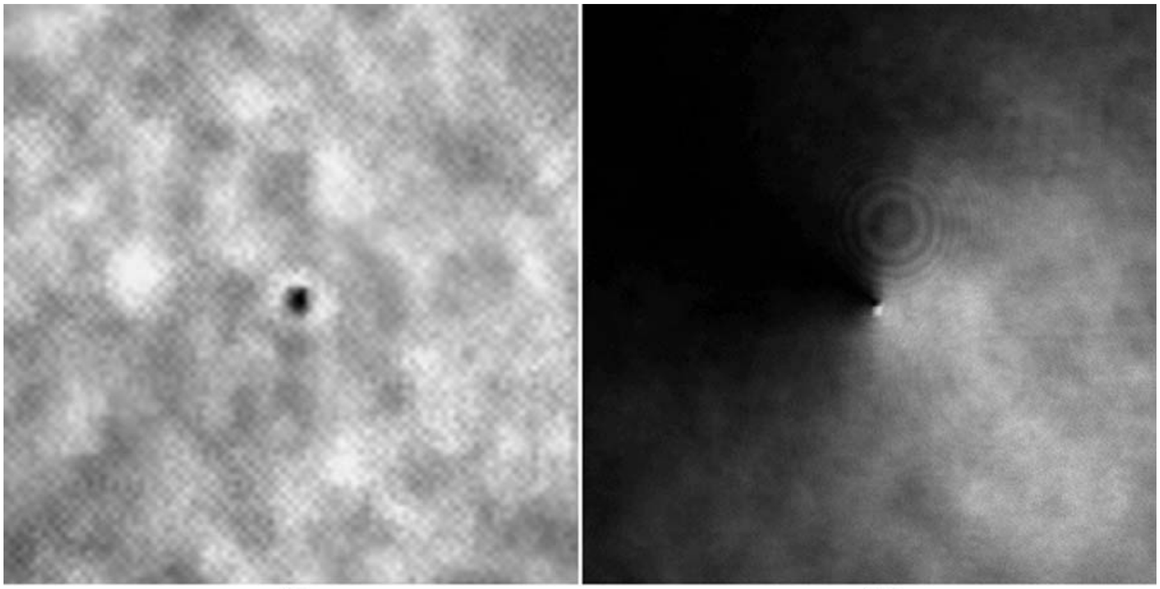
(a) (b)

Figure 3.9: Reproduction of the object beam from the hologram shown in figure 3.7. Image (a) shows the intensity pattern. The size of the cortex core, which can clearly be seen, is determined by the projection optics. For image (b), the object beam was interfered with a copropagating reference beam with a plane phase, in a Mach-Zehnder interferometer.

projection optics and is not given by the hologram itself.
To make the phase of the beam with orbital angular momentum visible, a Mach-Zehnder interferometer (see [38], page 411) was built. The hologram was placed into one arm and a first order was projected onto an image (camera) plane. As a reference beam a Gaussian beam with no phase variation in every crossection perpendicular to the propagation direction was chosen. The resulting intensity in the image plane can be seen in figure 3.9 (b). As expected there is a region where the phases interfere constructively, and a region of destructive interference on the opposite side of the vortex, which is positioned at the center of the image. If the position of the hologram in the direction of propagation of the light beam is changed, the regions of constructive/destructive inteference can be seen to move. For the first order beam oviously a position change of λ amounts to a phase change of 2π, so that the region of constructive interference moves the whole way around the vortex center back to the original position.
Two other holograms for vortex patterns are shown in figure 3.10. One for a four-vortex beam with all vortices spinning in the same direction (3.10 (a)), and a hexagonal pattern of vortices spinning all in the same direction (3.10 (b)).

The result of projecting the holograms of figure 3.10 is shown in figure 3.11 and 3.12. The respective location of the vortex centers is the same in all pictures. Figure parts (a) are always the intensities in the image planes; parts (b) show the interference pattern in the Mach-Zehnder interferometer. The region of small intensity at the center of a vortex is bigger for a vortex with higher charge, as can be seen in figure 3.11 (a), where the upper row vortices have charge 1 (left) and charge 2 (right). In the lower row are vortices with charges 4 (left) and 8 (right).

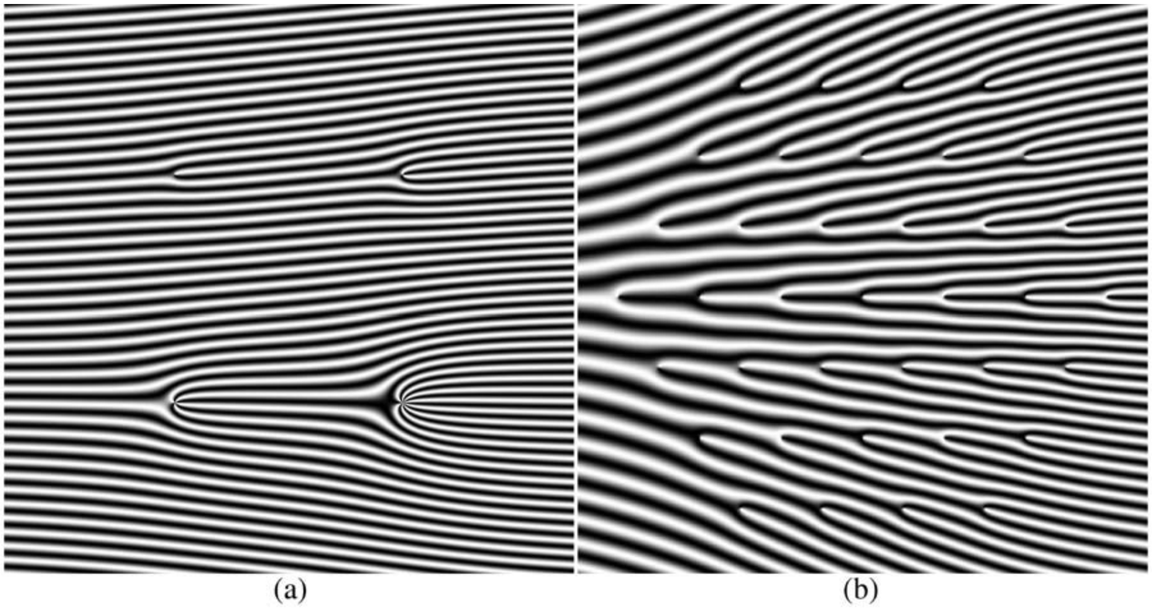

Figure 3.10: Calculated greyscale holograms for multiple vortex light beams. (a) differently charged vortices, (b) hexagonal vortex pattern. In the real chrome mask holograms made, the angle θ between object and reference beams was chosen larger. This results in a smaller line spacing compared to the vortex spacing. All chrome masks were of the same size and calculated for the same angle $\theta \approx 2.5°$. The resulting line spacing can be seen in figure in 3.7.

Depth of Focus for hologram projection

When projecting a hologram onto a cloud of atoms, the image plane needs to be positioned at the center of the cloud. Since no 2D gas is used in the experiments described in this thesis, the atoms at different positions along the direction of propagation z of the light see different intensity pattern of the light field due to the depth of focus of the projection system. For $d = \lambda$ the phase shift amounts to 2π.

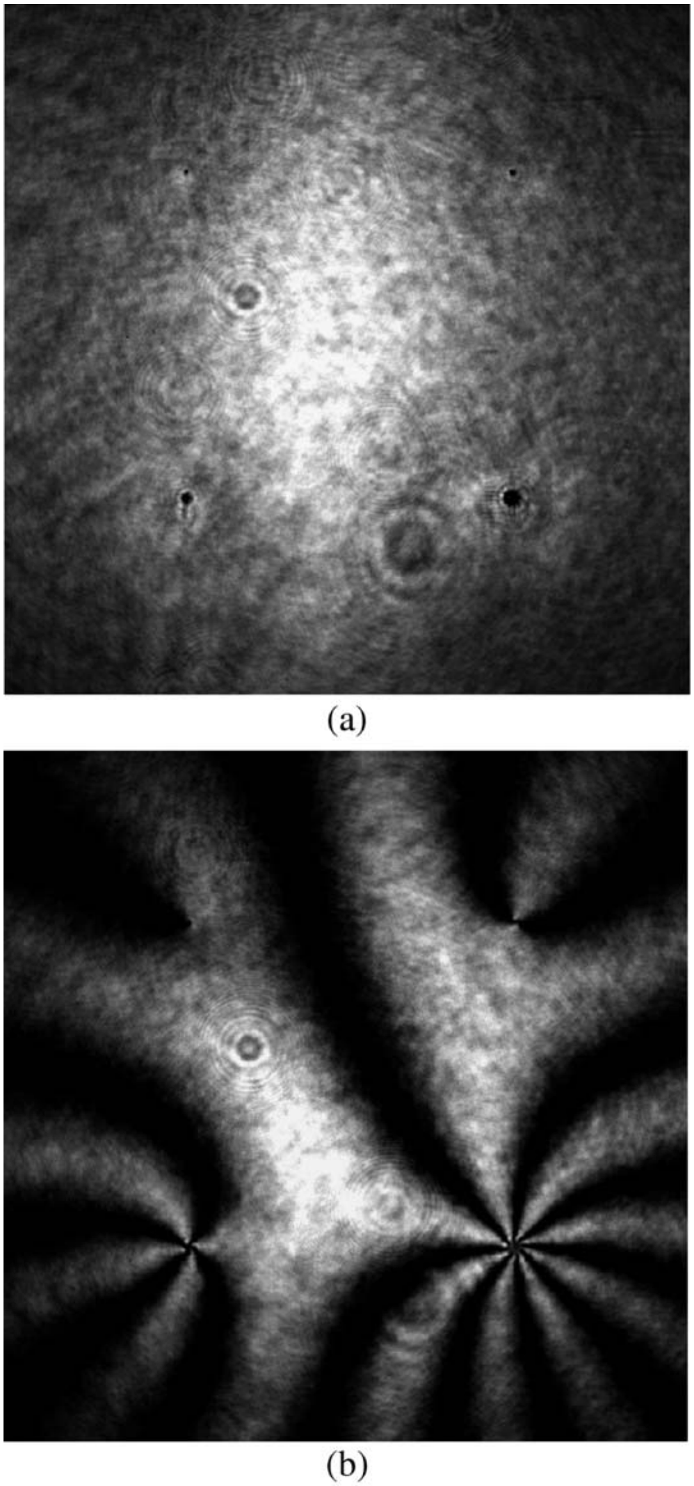

Figure 3.11: First order beam of a hologram of the type shown in 3.10(a). (a) intensity, (b) interference pattern. Both pictures are taken in the same way as described for figure 3.9.

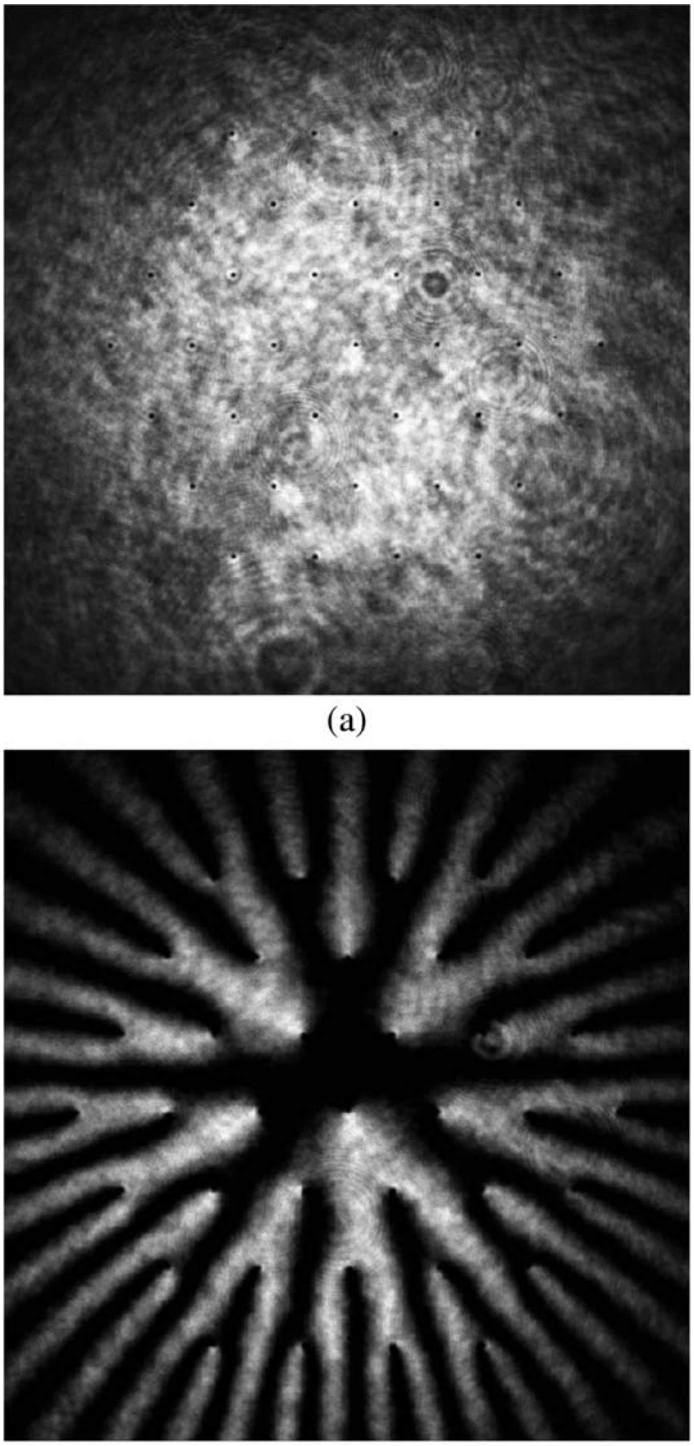

(a)

(b)

Figure 3.12: First order beam of a hologram of the type shown in 3.10(b). (a) intensity, (b) interference pattern. Both pictures are taken in the same way as described for figure 3.9.

As shown in chapter 4, different intensites lead to different Rabi frequencies Ω_{eff} for the Raman transitions at different locations in the beam and therefore limit maximum achievable population transfer to the state with orbital angular momentum. Depth of focus therefore limits the usability of holograms for projecting vortex patterns in 3 dimensional clouds.

The change of the light fields at different z-positions in the cloud can be computed using an input-output relation obtained from the transfer function of free space (see [28], pages 116-120).

$$\mathscr{H}(\nu_x, \nu_y) = e^{\left(-2\pi i\sqrt{\frac{1}{\lambda^2}-\nu_x^2-\nu_y^2}\; d\right)} \tag{3.11}$$

Is the function by which the amplitude of a plane wave in crossection $f(x, y, z = z_0)$, with spatial frequencies ν_x, ν_y, needs to be multiplied to obtain the amplitiude $f(x, y, z = z_0 + d)$ in another crossection $z + d$. This is valid for $1/\lambda^2 > \nu_x^2 + \nu_y^2$. By expanding an arbitrary input amplitude in plane $z = z_0$ in plane waves, the output amplitude at another position $z = z_0 + d$ can be calculated. This yields the input-output relation

$$f(x, y, z = z_0 + d) = \int d\nu_x d\nu_y \; \mathscr{H}(\nu_x, \nu_y) F(\nu_x, \nu_y) exp[-i2\pi(\nu_x x + \nu_y y)] \tag{3.12}$$

used to calculate the field amplitudes dependent on the position z. Here $F(\nu_x, \nu_y)$ is the Fourier transform of the input function $f(x, y, z = z_0)$ and the integrals transform back to position space to yield the field amplitudes in crossection $z_0 + d$.

Figure 3.13 shows a calculation for the intensity distribution around the image plane $z_0 = 0$ when projecting the hologram for the hexagonal vortex pattern shown in 3.10 (b). The calculation used equation 3.12 and assumed our diffraction limited projection optics with a numerical aperture of 0.55 was used. For the two Fourier transforms needed for this calculation, a list of values was first computed. This list was then discretely transformed by a Fast Fourier transform algorithm.

Clearly, a rapid change in the intensity pattern can be seen. Also, the centerpoints of the vortices do not stay at the same x, y coordinates, but rotate around the center of the structure. A spread of the vortex structure can also be seen, resulting in larger distance between vortices and a larger region of small intensity close to the vortex cores. For very large distances d the patterned structure of the beam disappears and a single multiple charged vortex appears. The charge of this vortex will then be the total orbital angular momentum contained in the beam - as required by angular momentum conservation.

The distance between vortices in the image plane ($d = 0$) of figure 3.13 was set to $4\mu m$. With this projection optics the dark region close to a vortex center is computed to be about $1\mu m$ in diameter in the ($d = 0$) image plane.

Compared to the size of a typical Bose-Einstein Condensate, which is around $30\mu m$ in a usual harmonic trap, it can be seen that a very good projection system is needed to project high filling factors of vortices. The use of a high numerical aperture will however restrict the system to 2 dimensions, as can be estimated from the depth of focus calculations described here.

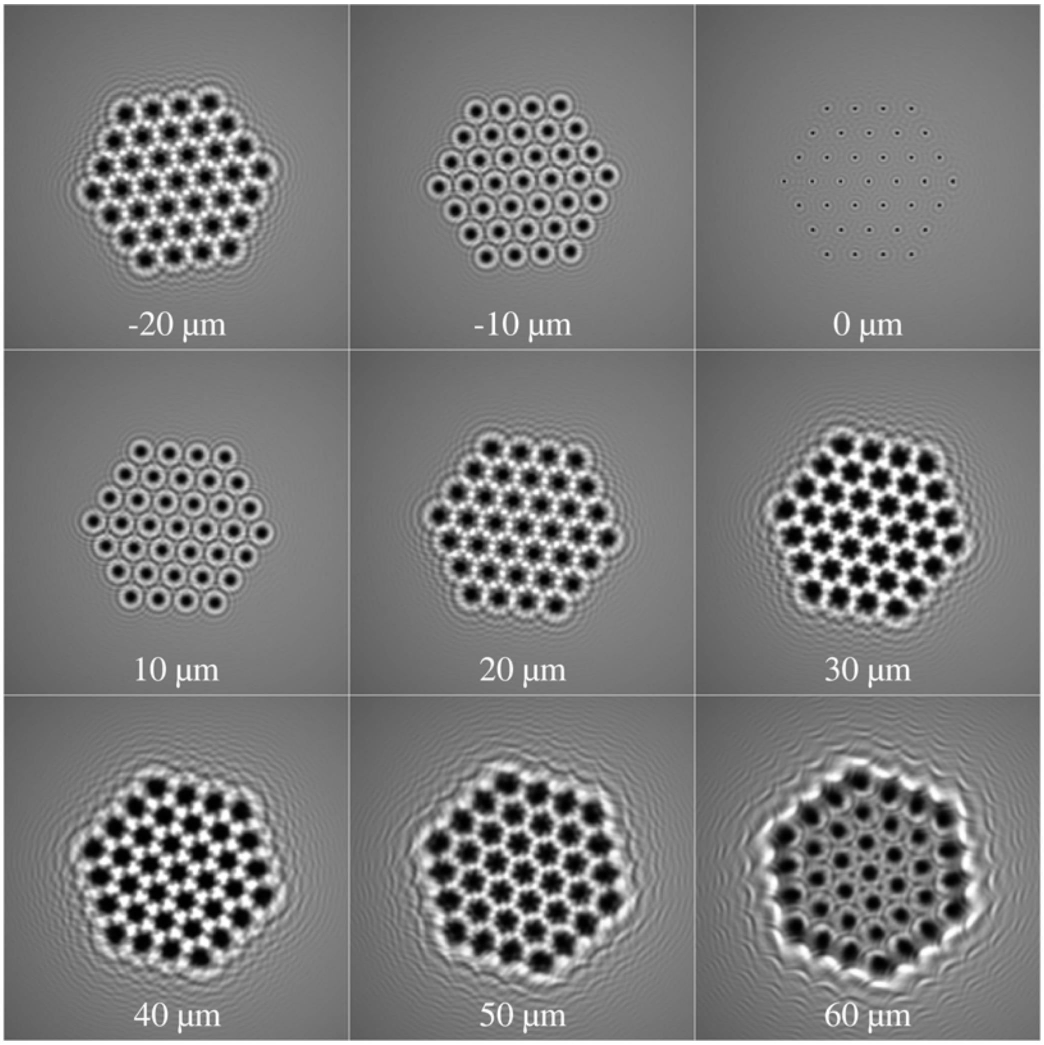

Figure 3.13: Projection of the hexagonal vortex pattern. Shown is the intensity in different planes $z = z_0 + d$ for values of d between $-20\mu m$ and $+60\mu m$. $d = 0$ specifies the image plane, where the vortex spacing is chosen to be $4\mu m$ for this calculation.

Chapter 4

Raman Transitions

Raman transitions provide a way to coherently transfer atoms between different quantum states. This state can be a different internal state and/or a different momentum state, characterized by a transferred momentum of $\hbar(\mathbf{k}_1 - \mathbf{k}_2)$, where $\mathbf{k}_1$ and $\mathbf{k}_2$ are the wave vectors of the respective light fields 1 and 2.

Atoms in a Bose-Einstein Condensate can be transfered into a vortex state, if one or both of the two light fields driving the Raman transition is carrying orbital angular momentum. A stimulated Raman transition is a process for which two light fields are needed. The atoms that undergo a Raman transition absorb a photon from one light field and reemit it into the other light field. Thus, if a photon with angular momentum is absorbed, but the stimulated emission to the other light beam demands a photon without angular momentum, the angular momentum quantum stays with the atom.

This chapter presents results from a description of Raman transitions in a three-level system in Λ-configuration and the laser setup that was build to drive Raman transitions in Rubidium 87 atoms. Spontaneous emission rates due to the light fields present during the process is compared to the Raman transfer rates. This is an important measure for the coherence of the process.

4.1 Raman transitions in the Λ-level configuration

4.1.1 Treatment as an effective two level system

Consider a 3 level system with states $|g\rangle, |e\rangle, |i\rangle$ and two light fields present as shown in figure 4.1. In a semi-classical description, the electric field, with both light fields $\mathbf{E}_1$, $\mathbf{E}_2$ of frequencies ω_1 and ω_2 present, can be written as

$$\mathbf{E} = \mathbf{E}_1 \cos(\mathbf{k}_1 \cdot \mathbf{x} - \omega_1 t + \phi_1) + \mathbf{E}_2 \cos(\mathbf{k}_2 \cdot \mathbf{x} - \omega_2 t + \phi_2) \tag{4.1}$$

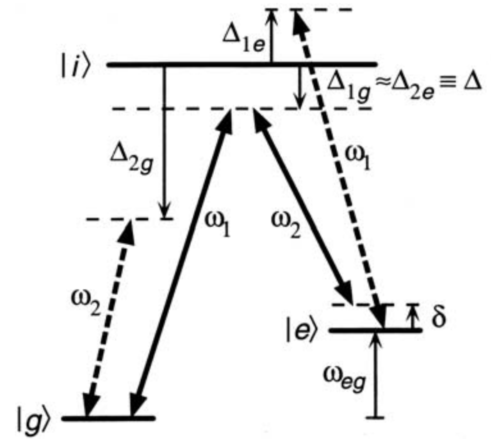

Figure 4.1: Three level system in Λ-configuration. The Δs are single photon detunings, δ is the two photon detuning. Raman transitions are driven between the levels $|g\rangle$ and $|e\rangle$. This figure is taken from [39]

Taking only electric dipole transitions into account, the semi-classical Hamiltonian of the system is

$$H = \frac{\mathbf{p}^2}{2m} + \hbar\omega_e|e\rangle\langle e| + \hbar\omega_i|i\rangle\langle i| + \hbar\omega_g|g\rangle\langle g| - \mathbf{d}\cdot\mathbf{E} \tag{4.2}$$

with the initial momentum $\mathbf{p}$ of the system, the resonant single photon transition frequencies $\omega_{g,i,e}$ to the respective levels and the electric dipole operator $-\mathbf{d}\cdot\mathbf{E}$. The light frequencies are taken to be nearly resonant, with a common detuning Δ, to precision δ, from the excited state, where δ is called the two photon detuning. Thus the difference between ω_1 and ω_2 is roughly ω_{eg}, which is the resonant transition frequency between the levels $|g\rangle$ and $|e\rangle$. The single photon detunings of light field 1 from levels $|e\rangle$ and $|i\rangle$ and light field 2 from levels $|g\rangle$ and $|e\rangle$ that are also shown in figure 4.1 contribute to the spontaneous emission rates, that introduce decoherence into the system, which are calculated later.
The single photon Rabi frequencies are defined as

$$\Omega_g = -\frac{\langle i|\mathbf{d}\cdot\mathbf{E}_1|g\rangle}{\hbar}, \qquad \Omega_e = -\frac{\langle i|\mathbf{d}\cdot\mathbf{E}_2|e\rangle}{\hbar} \tag{4.3}$$

and can be evaluated using the Wigner-Eckart theorem (see e.g. [40]). In the limit of far detunining $\Delta >> \Omega_g, \Omega_e$ and neglecting spontaneous emission, the third level $|i\rangle$ can be adiabatically eleminated [41], so that the system behaves like a 2 level system which is cycling between ground state $|g\rangle$ and excited state $|e\rangle$. The Rabi frequency for this transition in a frame rotating with ω_{eg} is

$$\Omega_r = \sqrt{\Omega_{eff}^2 + (\delta - \delta^{AC})^2} \tag{4.4}$$

with the two photon Rabi frequency

$$\Omega_{eff} = \frac{\Omega_e^* \Omega_g}{2\Delta} e^{i(\phi_1 - \phi_2)} \tag{4.5}$$

In Ω_r, several other effects have been taken into account:
Since the linewidth of a Raman transition is small, the effects of an initial momentum $\mathbf{p}$ of the system and the momentum transfer of the light itself cannot be neglected. Taking this into account, the two photon detuning becomes

$$\delta = (\omega_1 - \omega_2) - \left(\omega_{eg} + \frac{\mathbf{p} \cdot \mathbf{k}_{eff}}{m} + \frac{\hbar |\mathbf{k}_{eff}|^2}{2m} \right) \tag{4.6}$$

where $\hbar \mathbf{k}_{eff} = \hbar(\mathbf{k}_1 - \mathbf{k}_2)$ is the effective momentum transfer by the Raman transition to the system.
If the single photon Rabi frequencies are not the same, this causes a differential AC-Stark shift between the levels, which can be approximated by

$$\delta^{AC} = \frac{|\Omega_e|^2}{4\Delta} - \frac{|\Omega_g|^2}{4\Delta} \tag{4.7}$$

where only influence of ω_1 on state $|g\rangle$ and ω_2 on $|e\rangle$ has been considered for simplicity. For the expansion coefficients in the rotating frame $c_{e,\mathbf{p}+\hbar\mathbf{k}_{eff}}$ and $c_{g,\mathbf{p}}$, associated with the levels $|g\rangle$ and $|e\rangle$, the well known solution of the optical bloch equations for a two level system, which is gained by making the rotating wave approximation, can be used to obtain

$$\begin{aligned} c_{e,\mathbf{p}+\hbar\mathbf{k}_{eff}}(t_0+\tau) &= e^{-i(\Omega_e^{AC}+\Omega_g^{AC})\tau/2} e^{-i\delta\tau/2} \Bigg[c_{e,\mathbf{p}+\hbar\mathbf{k}_{eff}}(t_0) \Bigg(\cos\left(\frac{\Omega_r \tau}{2}\right) \\ &+ i \frac{\delta - \delta^{AC}}{\Omega_r} \sin\left(\frac{\Omega_r \tau}{2}\right) \Bigg) + c_{g,\mathbf{p}}(t_0) e^{-i(\delta t_0 + \phi_{eff})} \Bigg(-i \frac{\Omega_{eff}}{\Omega_r} \sin\left(\frac{\Omega_r \tau}{2}\right) \Bigg) \Bigg] \end{aligned} \tag{4.8}$$

$$\begin{aligned} c_{g,\mathbf{p}}(t_0+\tau) &= e^{-i(\Omega_e^{AC}+\Omega_g^{AC})\tau/2} e^{i\delta\tau/2} \Bigg[c_{e,\mathbf{p}+\hbar\mathbf{k}_{eff}}(t_0) e^{i(\delta t_0 + \phi_{eff})} \Bigg(-i \frac{\Omega_{eff}}{\Omega_r} \\ &\times \sin\left(\frac{\Omega_r \tau}{2}\right) \Bigg) + c_{g,\mathbf{p}}(t_0) \Bigg(\cos\left(\frac{\Omega_r \tau}{2}\right) + i \frac{\delta - \delta^{AC}}{\Omega_r} \sin\left(\frac{\Omega_r \tau}{2}\right) \Bigg) \Bigg] \end{aligned} \tag{4.9}$$

If the system is in the ground state at $\tau = 0$, the propability at τ to find it in the excited state is thus

$$|c_{e,\mathbf{p}+\hbar\mathbf{k}_{eff}}(t_0+\tau)|^2 = \frac{|\Omega_{eff}|^2}{\Omega_r^2} \sin^2\left(\frac{\Omega_r \tau}{2}\right) \tag{4.10}$$

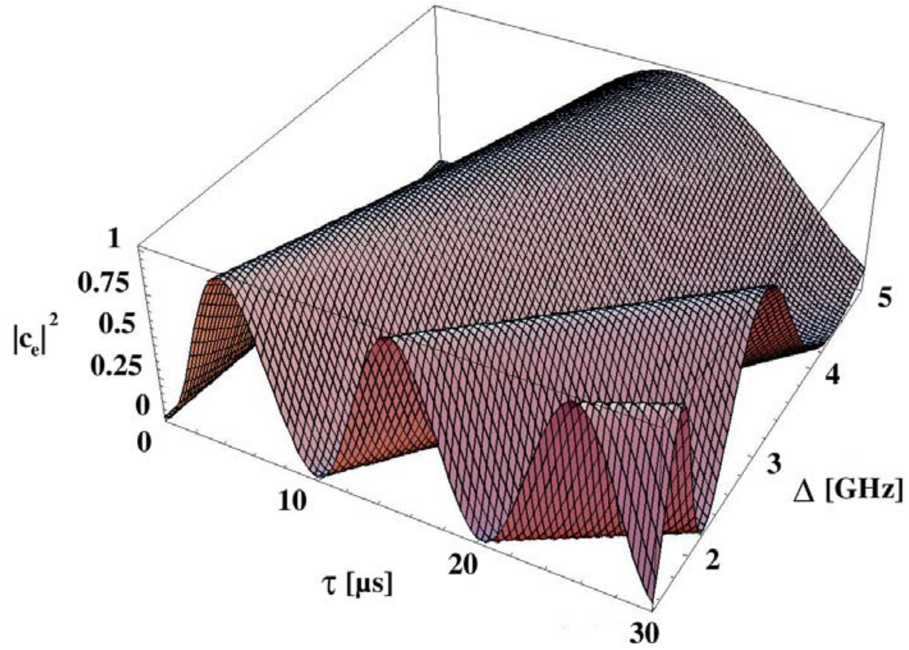

Figure 4.2: Rabi flopping of the system: Occupance of the excited state as a function of detuning and time. The intensity in this calculation chosen as $9\mu W/\pi(75\mu m)^2$, a value that is close the one used in the vortex experiments described in chapter 6.

Figure 4.2 shows this behaviour of the system, which is called Rabi flopping. The amplitude of oscillation does not decrease, since spontaneous emission and other processes that introduce decoherence are neglected in equation 4.10 which was used to calculate this graph. Also two-photon resonance was assumed, which means $|\Omega_{eff}|^2 = \Omega_r^2$.

Coherence and the Bloch sphere picture

The dynamics of the effective two level system can be nicely displayed in the Bloch sphere picture [42, 41]. Here, the state of the system is described by a vector on a unit sphere as shown in figure 4.3. In this picture, a vector in the positive z-direction is identified with the excited state $|e\rangle$; a vector in the negative z-direction with the ground state $|g\rangle$. States in between describe superposition states of the system, where the azimuthal angle represents the phase of the state. For example, a vector in the x-y plane describes a 50-50% superposition state with phase $e^{i\phi}$ where ϕ is the azimuthal angle.
Equations 4.9 describe the dynamics of the effective two level system as seen from a

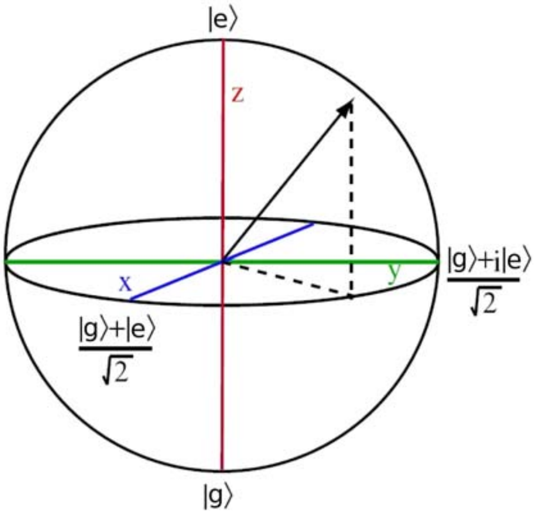

Figure 4.3: Bloch Sphere. This is a modified version of a picture taken from [41].

frame rotating with angular frequency ω_{eg}. In the Bloch sphere picture this means viewing the vector that represents the state of the system from a frame rotating with this angular frequency about the z-axis. The Bloch vector is found to follow exactly the same dynamics as a magnetic dipole vector precessing in a magnetic field. Expressing the vector as

$$\mathbf{S} = \begin{pmatrix} |g\rangle\langle e| + \ |e\rangle\langle g| \\ -i|e\rangle\langle g| + i|g\rangle\langle e| \\ |e\rangle\langle e| - \ |g\rangle\langle g| \end{pmatrix} \tag{4.11}$$

the Hamiltoninan for the system in the rotating frame can now be rewritten. In the Heisenberg picture, this leads to the equations of motion

$$\frac{d}{dt}\mathbf{S} = \mathbf{\Omega}(t) \times \mathbf{S} \tag{4.12}$$

for the vector on the Bloch sphere. Where

$$\mathbf{\Omega}(t) = \begin{pmatrix} -2Re(\Omega_{eff}(t)) \\ -2Im(\Omega^*_{eff}(t)) \\ -\delta \end{pmatrix} \tag{4.13}$$

is the axis around which the Bloch vector precesses at time t, for the case $|\Omega_{eff}|^2/\Omega_r^2 = 1$, where the system is initially at rest $\mathbf{p} = 0$, the two light fields are copropagating $\mathbf{k}_{eff} \approx 0$ and the single photon Rabi frequencies 4.3 are the same.

Suppose at time t_0, the system is in a superposition state and our goal is to transfer it completely into the excited state. From equation 4.10 clearly follows that we can only achieve that for $|\Omega_{eff}|^2/\Omega_r^2 = 1$. But that is not all that matters: The orientation of the rotation axis $\mathbf{\Omega}$ depends on the relative phase between the two driving light fields (see the definition of Ω_{eff}, equation 4.5). If the two photon detuning δ is chosen to be zero, the rotation axis $\mathbf{\Omega}$ lies in the x-y plane, but only for one specific orientation will the Bloch vector pass through the state $|e\rangle$. An example for a case, when the relative phase of the two light fields is not oriented in a right way with respect to the bloch sphere vector to achieve complete transfer to the excited state is shown in figure 4.4.

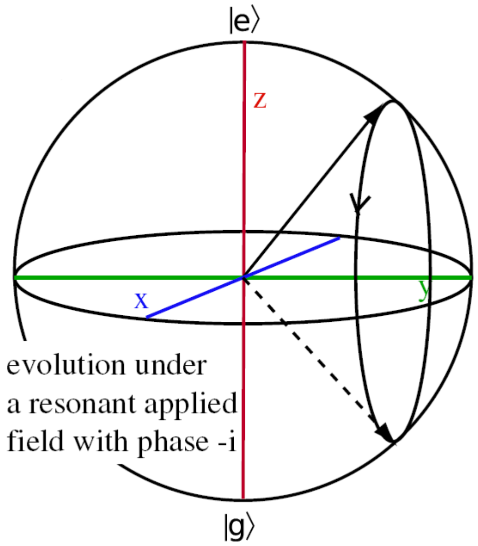

Figure 4.4: If the relative phases of the light fields don't match the phase of the Bloch vector, no complete transfer to the excited state can be achieved. If the Bloch vector is originally in the y-z plane at t_0, $\mathbf{\Omega}$ needs to lie on the x-axis inorder to achieve complete transfer. The picture is taken from [41]

The considerations just presented make it clear, that the relative phase of the the two driving light fields must not vary much during the pulse duration, even for the practically interesting case where we want to transfer the system from ground to excited state (here only the stability matters, since $|g\rangle$ is always orthogonal to $\mathbf{\Omega}$ when the light fields are two-photon resonant). Since π-pulses are usually rather short, this is not so hard to achieve, however. More demanding is the phase stabilization, if a sequence of pulses (Ramsey sequence) is applied. In this case the relative phase between the light fields must be stable for the whole sequence of pulses when a superposition state of a specific phase is supposed to be changed in a defined way.

4.1.2 Spontaneous emission

During a stimulated Raman transition, the system absorbs a photon from one light field, being "lifted" to level $|i\rangle$ and reemits it again to the other light field by stimulated emission. During a time interval τ_0, that is given by the energy-time uncertaincy relation $\tau_0 \simeq 1/\Delta$, the system also has the option to spontaneoulsy reemit the photon. This is clearly unwanted, since atoms in a cloud that undergo the transition can be lost to other levels. But even worse, spontaneous emission is an incoherent process. To induce vortices, a defined momentum transfer is needed, while spontaneous emission gives random momentum kicks to an atom. Therefore the ratio of spontaneous emission to stimulated emission from the upper level has to be minimized, which can be accomplished by choosing the detuning Δ to be large.
The spontaneous scattering rate Γ_{sc} may be estimated as

$$\Gamma_{sc} = -\frac{\langle \dot{\mathbf{d}} \cdot \mathbf{E} \rangle}{\hbar\omega} \approx \frac{3\pi c^2}{2\hbar\omega_0^3}\Gamma \sum_j I_j \left| \frac{\langle F1; m_F q | F1; F' m'_F \rangle_j}{\Delta_j} \right|^2 \tag{4.14}$$

which can be obtained from a simple oscillator model of an atom interacting with a light field [43, 44]. Here ω_0 is the resonance frequency of the oscillator model, $I_j = 1/2\epsilon_0 c|E|^2$ the intensity of the respective light field and Γ the damping constant of the oscillator model (decay rate). The scattering rates of all levels with the common decay rate are summed up, taking their respective transition strengths, given by the Clebsch-Gordan coefficients in the numerator, and detunings from resonance in the denominator, into account. In the Clebsch-Gordan coefficient, the spin of a photon is added to the total angular momentum of the atom.

Optimization of coherent transfer rates

Spontaneous emission is often a problem when high transfer rates are needed. Stimulated Raman Adiabatic Passage and Landau-Zener Passage are schemes for applying the coherent light fields separately [45, 41]. These allow rather stable transfer rates, independent of the pulse lengths. If the pulse lengths are very short (e.g. due to strong transitions), the problem of controlling such a short pulse can also be solved in this manner. The basic idea for these schemes can be understood in the dressed atomic states picture. It is achieved by adiabatically moving a dressed atomic state from one bare state to another, and thereby changing the state of the system.
For the specific setup with which the experiments for this thesis were performed, the transfer rates and spontaneous emission rates were however not limiting. Since the Raman pulses were applied during time of flight, while the atoms were already falling, fluctuations were tolerated to get faster transfer rates.
However, if the setup is used with fewer atoms that one wants to prepare in very

defined states, as might be needed in the optical lattice simulator, the techniques mentioned above might be interesting.

4.2 Raman laser setup

Our experiments are performed using Rubidium 87 as a bosonic particle. The Raman setup that was built in the course of the work for this thesis, can be used to drive transitions between the hyperfine ground states $|5^2S_{1/2}; F = 1, 2\ m_F\rangle$ and all magnetic sublevels of these states (for transitions that satisfy the selection rules). By choosing the propagation direction of the Raman beams with respect to each other, linear momentum can be transfered to the atoms undergoing the transitions. This can, for example, be used for Bragg diffraction experiments [46]. The transitions are driven via the intermediate states $|5^2P_{1/2}; F = 1, 2\ m_F\rangle$ using the $D1$ transition (see figure 4.5). The interaction with both levels is determined by the detuning Δ, which is usually bigger than the $5^2P_{1/2}$ hyperfine splitting of $816MHz$. Nevertheless, a very good approximation to a three level system can be constructed for some transitions. This is accomplished by choosing the polarizations in a way that the selection rules prevent transitions via the $|5^2P_{1/2}; F = 1\ m_F\rangle$ states.
Since the availability of Electro-Optical Modulators (EOM) [28] that can handle modulation frequencies of higher than $10GHz$, it is possible to build such a setup, even for transitions changing the hyperfine state, with little complexity. For our case, the hyperfine splitting of the ^{87}Rb $5^2S_{1/2}$ ground state is $6.8GHz$, so the setup needs to provide two coherent light fields of this frequency difference.
It is possible to build two lasers that need to be phase locked and kept at the difference frequency, to provide these light fields. However the use of an EOM makes the whole setup much less complex, since the light of the same laser can be split up and is therefore already inherently coherent. The phase stability between the light fields therefore depends on the phase stability of the oscillator that generates the modulation signal driving the EOM. Considerations about the phase stability of the microwave modulation frequency, will be given later in this section. When the signal is applied to the EOM, it will create side bands in the light fields, which are spaced by the modulation frequency.
For Zeeman state and momentum state changing transitions, which are at much lower frequency, the frequency difference is provided directly by AOMs.

4.2.1 Setup

Figure 4.6 shows a picture of the setup. The $795nm$ diode laser has an external cavity with a Littrow grating, which reflects the $1st$ order back into the diode and thus makes it run on one mode of the internal cavity. The details of this configuration

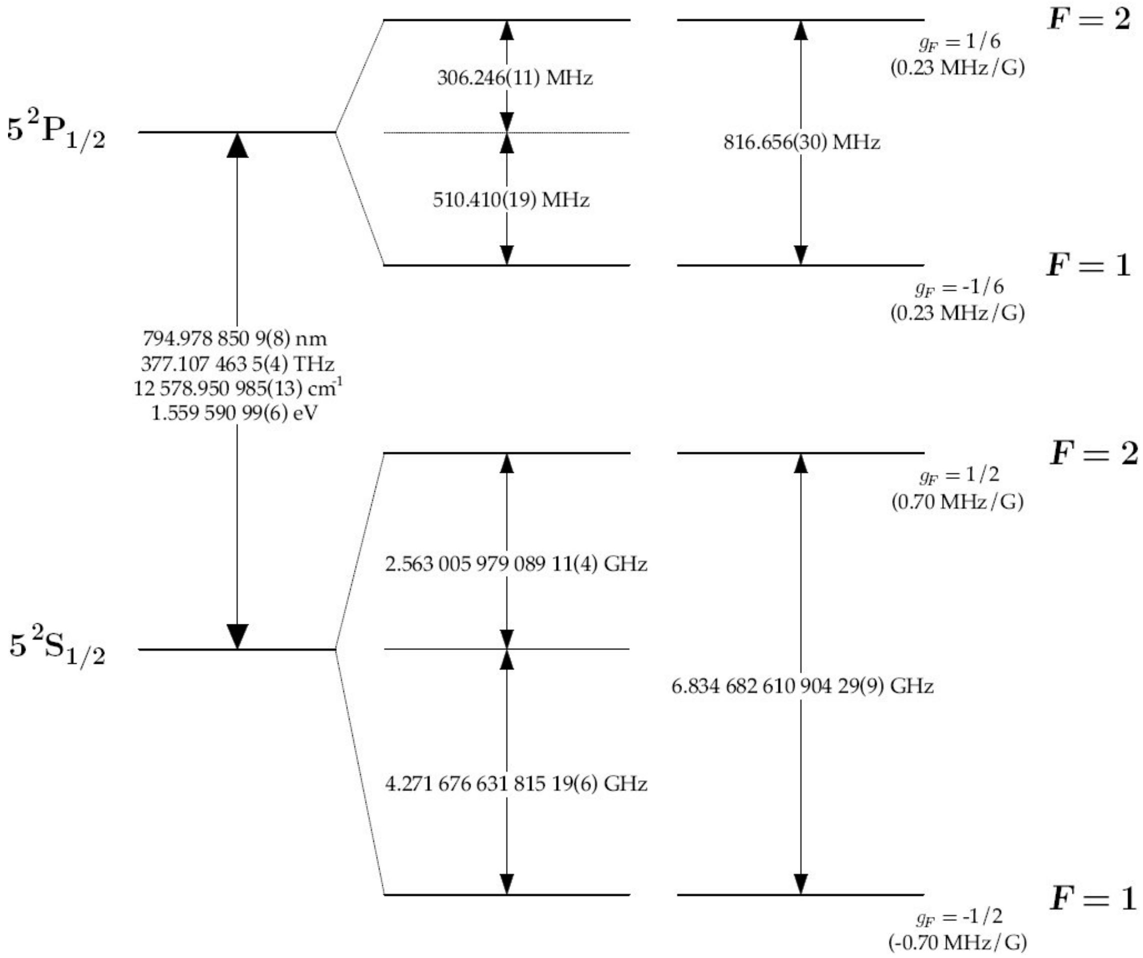

Figure 4.5: D1 level structure. With the setup described all possible transitions between the $5^2S_{1/2}$ magnetic and hyperfine levels can be driven. The graphic is taken from [47].

are explained elsewhere [48]. Following the main beam path (shown in red) through the setup, we pass an anamorphic prism pair that changes the output of the laser diode to an approximately circular beam profile and a faraday isolator that prevents back reflections from farther downstream affecting the laser diode.

At the next cube, the light for the lock signal generation and spectroscopy is split off. Looking downstream the main beam path, the vapor cell that contains both ^{87}Rb and ^{85}Rb isotopes can be seen to the right. Details of lock signal generation and saturation spectroscopy are described in [49] (lock signal) and [48] (saturation spectroscopy). From the lock signal an error signal is derived, which is fed back to the piezo that moves the Littrow grating, and keeps the laser at a constant frequency.

Along the main beam path then follows a telescope that changes the beam size to

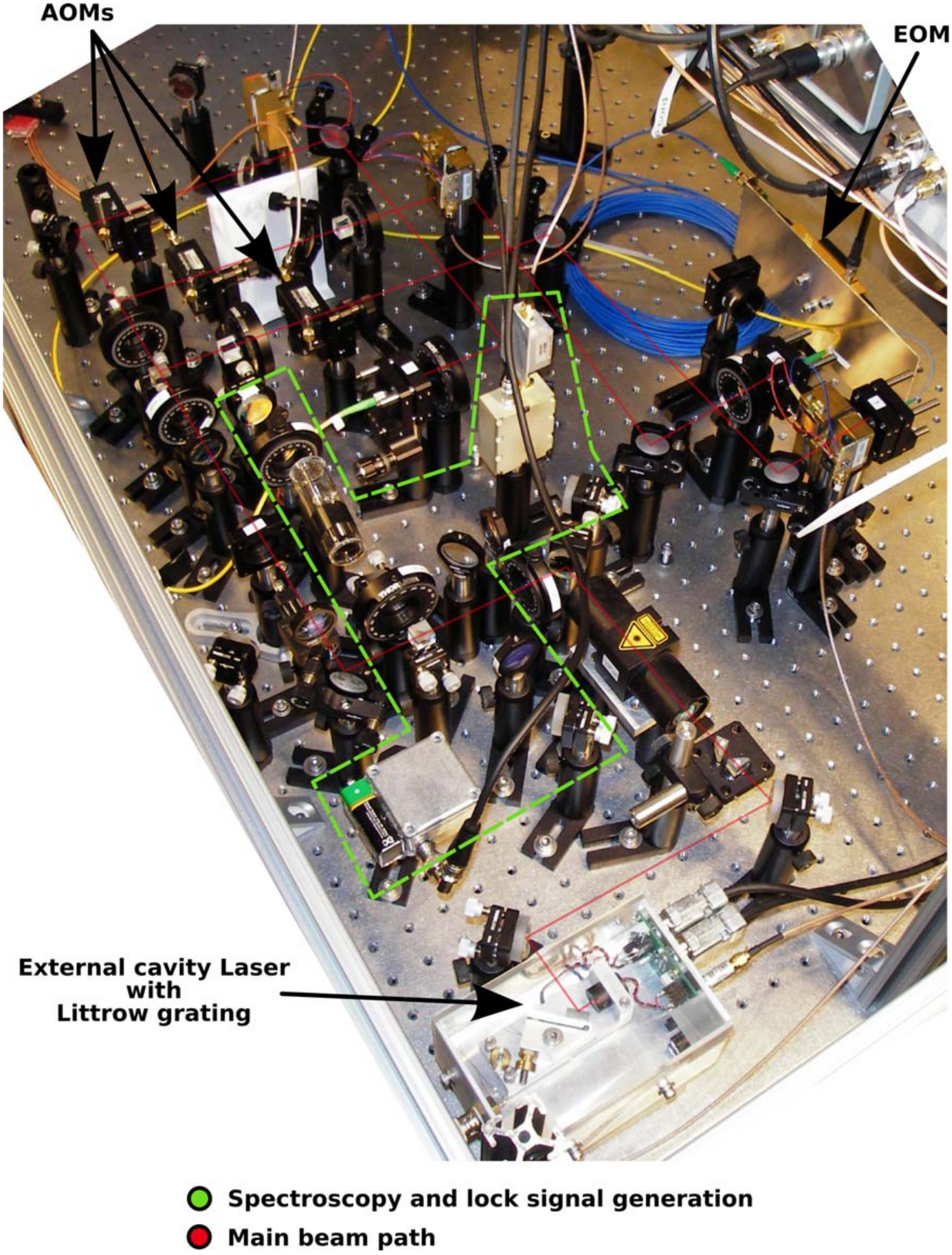

Figure 4.6: Raman laser setup

mode match the fiber coupling. Then the beam is split up into three, passing through two cubes. Each of the resulting beams pass through separate AOMs which are used to switch the beams on and off fast enough for Raman pulses and to change the frequency of the light by adding an RF-phonon to photons passing through it. After that, the beams pass through mechanical shutters, which guarantee good beam extinction and are fiber coupled. The EOM is a fibercoupled version, which is directly put in one of the fiber paths.

The core of the EOM fiber is $4\mu m$, which is also the size of the birefringent lithium niobate crystal used in it. Thus the electrodes between which the modulation signal is applied are only spaced by this distance. Consequently a high electrical field energy density can be achieved in the crystal even with a low total field energy. This makes the high efficiency even at modulation frequencies of up to $20GHz$ possible.

Through the fibers, the light passes on to a different table with the vacuum apperatus. One of the light beams passes through the hologram which is mounted on the other table together with the projection system for the light beams onto to the atoms. This part will be described in chapter 6.

4.2.2 Sideband intensity and oscillator stability for the EOM

Phase modulation

In an EOM the refractive index of a birefringent crystal is changed by a voltage that is put across it (see [28]). This means, that if a voltage is applied across the crystal, the light passing through it will experience a phase shift compared to $0V$ that is proportional to the voltage (for a linear modulator). When the voltage is time dependent, the light is phase modulated. The classical electrical field of the *light* for a sinusoidal modulation is

$$\mathbf{E} = \mathbf{A}\ e^{i(\omega t+\phi+B\cos(\omega_m t+\phi_m))} \tag{4.15}$$

where $\mathbf{A}$ is the light amplitude, ω is the carrier light frequency, ϕ the phase of the light without modulation at time $t = 0$, B the modulation amplitude, ω_m the modulation frequency and ϕ_m the phase of the modulation signal at time $t = 0$. Fourier transformation of expression 4.15 gives

$$\mathbf{E} = \mathbf{A}\sum_{n=0}^{\infty} i^n J_n(B) e^{i(\omega \pm n\omega_m t+\phi\pm n\phi_m)} \tag{4.16}$$

where the amplitude of the different frequency components are found to be Bessel functions with the amplitude of the modulation signal B as their argument. In our setup we want to use the first order sideband, the intensity of which we thus want to maximize. Figure 4.7 shows the intensity of the carrier light and the first two

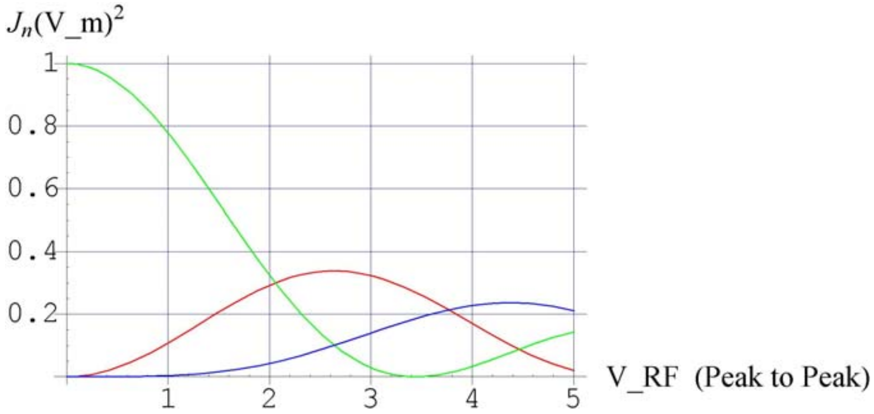

Figure 4.7: Intensity of the carrier (green), a single first order sideband (red) and a single second order sideband (blue) as a function of the modulation voltage amplitude.

sidebands as a function of peak-to-peak modulation amplitude. The source of the modulation frequency and the phase stability of it are treated in the next paragraph.

Oscillator stability

As explained, the modulation voltage needs to be phase and frequency stable in order to get reproducible Raman transfer rates with the laser setup. Thus the noise of the oscillator that puts out the modulation voltage for the EOM needs to be considered. The total noise of an oscillator has two contributions, amplitude noise and phase noise (see figure 4.8). The interesting quantity for this case is, how much the phase of the oscillator drifts during a pulse or pulse sequence, since that gives rise to a change in the rotation axis around which the Bloch vector precesses. Thus, amplitude noise is neglected in the following.
The root mean square drift $\langle\Delta\phi(t)\rangle$ of the oscillator phase after a time t can be calculated from the single sideband power spectrum $L(\Delta\omega)$ as

$$\langle\Delta\phi(t)\rangle = \sqrt{\frac{4}{\pi}\int_0^\infty d\Delta\omega\ L(\Delta\omega)\sin^2(\frac{\Delta\omega t}{2})} \tag{4.17}$$

where $\Delta\omega = \omega - \omega_0$ is the frequency off the carrier. $L(\Delta\omega)$ is a typical way to specify the noise for most oscillators. For a derivation of this formula, see [50].
In our setup, the $6.8GHz$ modulation signal is obtained from external multiplication of a $142MHz$ signal, derived from frequency synthesizer, by a factor of 48×. An approximate integration of the power spectrum given by the company using equation

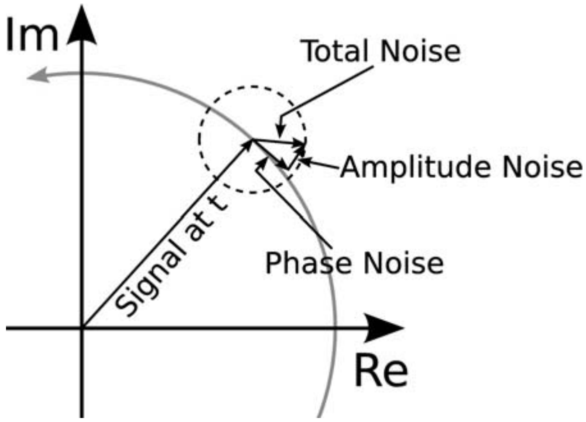

Figure 4.8: Amplitude and phase noise. Shown is the oscillator signal at a time t, which is rotating counter clock wise in the complex plane. The direction of phase noise amplitude is orthogonal to the direction of the signal amplitude and the amplitude noise.

4.17 gave $\langle \Delta\phi(10ms) \rangle \approx 30mrad$. The true phase drift might be slightly bigger, since the synthesizer produces the wanted ouput frequency from an internal oscillator, and the power spectrum specification of the company was given for multiples of the internal oscillator frequency only. Even so, the oscillator phase should still be stable enough to apply defined Ramsey sequences for which more than one pulse is applied during longer time intervals.

4.2.3 Complete Raman scheme

The Raman transitions we want to drive with the described setup are more complicated than the ones in the simplified description, given in section 4.1. In the first place, there are four levels that matter. Since we want to supress spontaneous scattering as much as possible, we need to choose a detuning that is around 3 times as big as the $5^2P_{1/2}$ level spacing. That means that both $5^2P_{1/2}$ hyperfine states contribute to the transition.

Also, since an EOM is used, all the sideband light frequencies and the carrier will be present (for maximum intensity of the first order sideband, see figure 4.7). A simplified scheme of the light fields present that contribute most to the Raman transition and spontaneous scattering is shown in figure 4.9. The wanted transition is driven via the first order of the EOM and the second "Beam 2" that does not contain sidebands. As can be seen from the figure, the backwards transition is possibly driven at the same time by the minus first order and Beam 2. This might lead to destructive interference, which is avoided in our setup by using the small linewidth of Raman transitions and the two photon detuning to our advantage. For that, the modulation

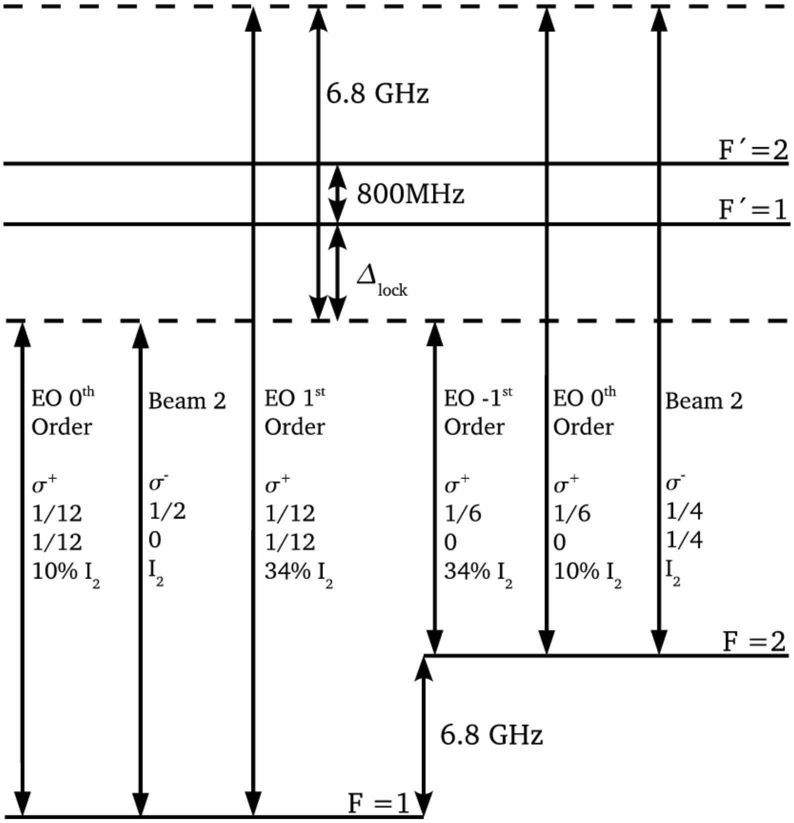

Figure 4.9: A simplified scheme of the light fields present. Shown are only the light fields that drive the transition and those that mainly contribute to spontaneous emission. For each of the light fields, the polarization, the square of the Clebsch-Gordan coefficients (upper one for $F' = 2$, lower one for $F' = 1$) for the respective transitions and the intensity compared to the beam without EOM is given. The frequency shifts due to the AOMs are not shown.

frequency of the EOM is chosen a little ($\sim 8MHz$) higher than the number shown in figure 4.5 for the hyperfine splitting. In beam 2 this shift is compensated by the AOM in its beam path. Since the minus first order of the EOM is shifted in the other direction, the two photon detuning for the backwards transition is around $16MHz$ - more than enough to prevent it from having any effect. Even with the shortest pulses we can control, the linewidth of the Raman transition is not much bigger than $100kHz$.

Our choice of polarizations shown in the picture is rather arbitrary and depends more on technical matters as for example mounts for coils that define quantization axes. The common detuning Δ is achieved by locking the laser to a ^{85}Rb transition.

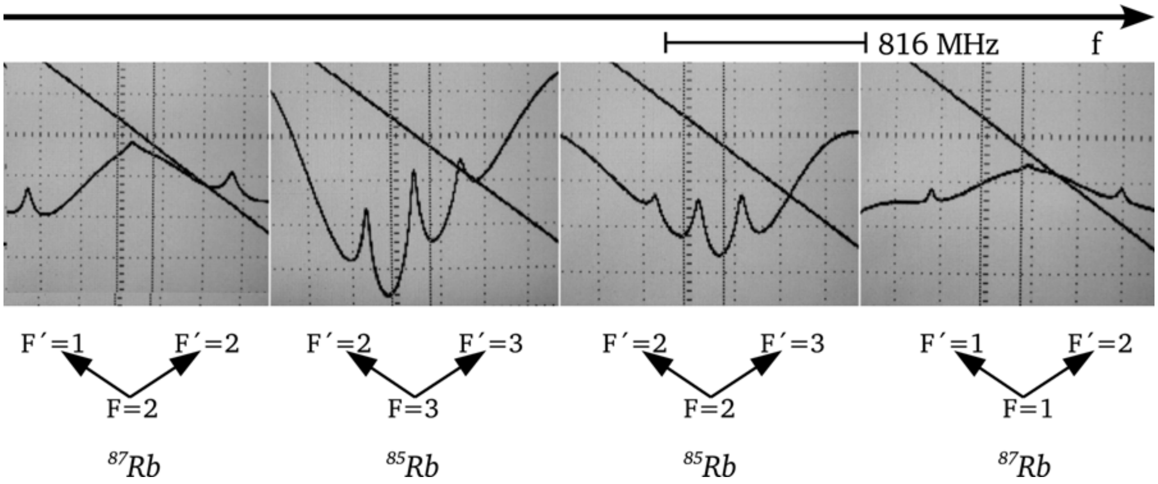

Figure 4.10: Saturation spectroscopy of the ^{87}Rb and ^{85}Rb lines as obtained from the laser setup. The ^{87}Rb lines are spaced so far apart, that they hardly fit in the same doppler curve, which is why there is almost no crossover peak visible. In our Ioffe-Pritchard trap, the atoms are prepared in state $|5^2S_{1/2}; F = 1 m_f = -1\rangle$. The detuning Δ_{lock} from the resonant transition $F = 1 \rightarrow F' = 1$ is achieved by locking to one of the ^{85}Rb lines. It follows from a calculation that Δ_{lock} can be chosen as $1848 MHz$, $2210 MHz$, $4885 MHz$, $5246 MHz$ or the 2 crossover peaks.

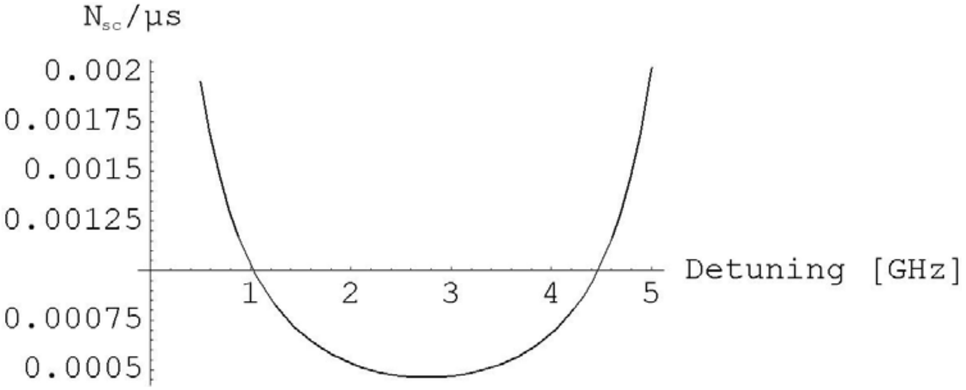

Figure 4.11: Spontaneous scattering rates to be expected per atom and μs. The detuning shown is Δ_{lock}, which is not the detuning for the Raman transition Δ.

The hyperfine splittings in ${}^{85}Rb$ are smaller by just the right amount to have a nice variety of detunings at hand. These can be calculated with (see [47])

$$\Delta E_{hfs} = \frac{1}{2} A_{hfs} K + B_{hfs} \frac{\frac{3}{2}K(K+1) - 2I(I+1)J(J+1)}{2I(2I-1)2J(2J-1)} \tag{4.18}$$

where

$$K = F(F+1) - I(I+1) - J(J+1) \tag{4.19}$$

From the calculation for ${}^{85}Rb$ and the numbers in figure 4.5 follow the possible detunigs Δ_{lock}. These and the saturation spectroscopy line shapes are shown in figure 4.10.

The spontaneous scattering rates, calcutated by summing up the scattering rates for all light fields using equation 4.14 are shown in figure 4.11. There is a minimum since, for a big detuning Δ_{lock}, the light fields from the upper level are beginning to become resonant again. This can be seen from figure 4.9.

Chapter 5

Projection and imaging

In this chapter, the projection system that was used to image the first diffraction order of a hologram onto a Bose-Einstein Condensate is described. It does not contain the final high NA objective, but was designed for the experiments described in chapter 6. Since the pictures and quantitative analysis shown in chapter 6 depend on absorption imaging, this technique is shortly described as well.

5.1 Projection setup

The projection setup for the holograms is shown is figure 5.1. In the foreground the chrome mask hologram can be seen. Along the beam path of the first order diffracted beam then follows a 1 to 1 imaging system in $4f$ configuration (for a description, see [28]). The $4f$ system consists of two lenses that perform a Fourier transform and a back transformation. The hologram is put in one focal plane of the first lens and its (finite aperture) Fourier transform appears in the second focal plane of this lens. The wanted first order vortex beam is filtered out by an aperture here and this selected light field is transformed back by the second lens of the $4f$ system. Thus in the second focal plane an image of the first order angular momentum beam appears. This image was demagnified by a telescope (not shown) and projected onto the atoms. The demagification was changed during the later experiments and will be specified in chapter 6. The first telescope lens, which was a $1000mm$ achromatic lens was mounted on a rail. With that it could be moved to focus the vortex beam in the plane of the atoms.

The light of the other 2 (Gaussian) beams is joined to the first order hologram beam by a non-polarizing beam splitting cube directly after the first lens of the $4f$ configuration. One of these light beams has passed through the EOM and contains the sideband shifted by $6.8GHz$. The other beam is a plain Gaussian (reference) beam which was used for the interference experiments with the vortex beams, which

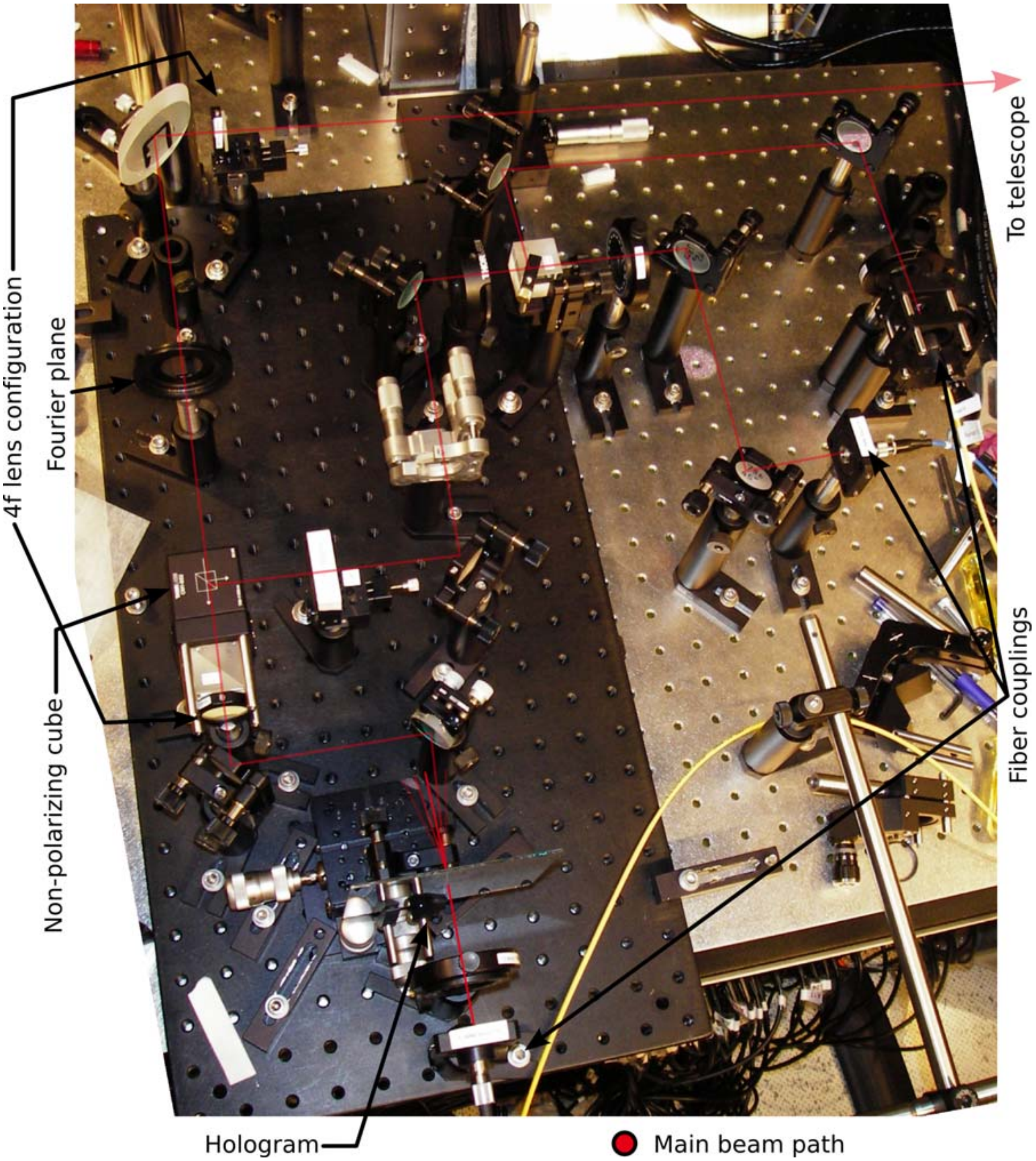

Figure 5.1: Projection setup for the hologram which can be seen in the lower part of the picture. In the Fourier plane of a $4f$ lens configuration, one first diffraction order of the hologram is selected by an aperture. Two Gaussian beams with orthogonal polarizations are made copropagating with the hologram beam.

are described in chapter 6. All the beams were aligned copropagating to interferometric precision by interfering two beams at a time. For the alignement, the EOM was switched off, the AOMs were set to the same frequency and polarizations were changed.

As this was done, the interference pattern was seen to change rather fast in time, even though the RF-signal for two of the AOMs were derived from the same oscillator. Most likely the long fibers that were used in the experiment and mechanical movement of the mounts lead to this. For Ramsey sequences, a more stable setup would need to be built, but for the short pulses that were applied in the experiments described in chapter 6, the stability was good enough. For this setup, the change in phase due to mechanical movements was clearly a much bigger effect than the instability due to the oscillator that was calculated in chapter 4.

Polarizations were adjusted to the ones shown in figure 4.9 in the following way: The light coming from the hologram passes a cube that polarizes it linearly. The other two light beams are joined in a polarizing beam splitting cube, thus having orthogonal polarizations. A $\lambda/2$ wave plate is used to make the polarization of the plain Gaussian (reference) beam the same as the vortex beam. Circular polarizations were obtained with a $\lambda/4$ wave plate, that turns the orthogonal polarizations of the EOM beam and hologram or plain gaussian beam into σ^+ and σ^-.

After time of flight, which was usually $17ms$ for the vortex experiments, the cloud was imaged onto a CCD camera using $D2$ $F = 2 \rightarrow F = 3$ light. The imaging setup consisted of two achromatic lenses magnifiying the image of the atoms. This magification was changed during the later experiments and will be specified in chapter 6. When imaging the $|5^2S_{1/2}; F = 1\ m_F = -1\rangle$ state, in which the atoms are originally prepared, $F = 1 \rightarrow F = 2$ repump light was additionally applied during imaging. For all vortex experiments, hyperfine structure changing transitions were used however and no repump light was applied in this case.

5.2 Absorption imaging of a Bose-Einstein Condensate

If a cloud of atoms is illuminated by a resonant or near resonant light beam, the scattering that occurs casts a shadow in the light beam. The light can then be imaged on a camera making the density profile in z-direction $\tilde{n}(x, y)$, of the cloud visible (if the imaging resolution is high enough). Thus, from measuring the optical density, dependent on the x and y positions in the plane, the real column density profile and the approximate number of atoms in the cloud can be computed.

A light beam with an intensity profile $I_0(x, y)$ is attenuated by

$$I(x, y) = I_0(x, y)e^{-D(x,y)} \tag{5.1}$$

when passing through the cloud with optical density $D(x,y)$ [44]. The optical density depends on the atomic column density

$$D(x,y) = 2\sigma_0 \frac{1}{1 + \frac{I}{I_{Sat}} + \frac{4\Delta^2}{\Gamma^2}} \tilde{n}(x,y) \tag{5.2}$$

where $\sigma_0 = \lambda^2/2\pi$ is the polarzation averaged resonant scattering cross section of the atoms, I the beam intensity, which is taken to be constant in the region of the atoms, I_{Sat} the saturation intensity of the respective transition, Δ the detuning of the light from resonance, and Γ the decay rate of the excited state.

$$D(x,y) = \max\left[0, A\Big(1 - \Big(\frac{x - x_c}{\sigma_x}\Big)^2 - \Big(\frac{y - y_c}{\sigma_y}\Big)^2\Big)^{\frac{3}{2}}\right] \tag{5.3}$$

Is taken as the approximate optical density function in our experiments, where $\sigma_{x,y}$ are the characteristic widths of the condensate. These and the peak optical density A are found as fit parameters. The total number of atoms N can be found from these parameters by integrating $\tilde{n}(x,y)$, which gives:

$$N = \frac{A\pi\sigma_x\sigma_y}{5\sigma_0}\Big(1 + \frac{I}{I_{Sat}} + \frac{4\Delta^2}{\Gamma^2}\Big) \tag{5.4}$$

As a concluding remark it needs to be mentioned, that for detuned imaging light, refraction of the condensate itself can change the optical density function, as observed in the camera plane, significantly. A detailed description of the expected images can be found in [51]. Different shapes of cloud shadows can be seen for red and blue detuned light. However, this effect is mostly observed, if the imaging system is not focused properly. Some of the shadows for detuned and defocused imaging can look very similar to the density profile of a vortex state, which can be annoying ...

Chapter 6

Experimental Results

In this last chapter, the first results of vortex projection and Raman setup experiments are presented. It is demonstrated that it is possible to transfer orbital angular momentum from a light beam to atoms in a Bose-Einstein Condensate. By interfering the atom wavefunctions of a vortex state with a constant phase one, it can directly be seen that the phase of the classical electromagnetic field of the light beams inducing the Raman transitions is stored in the atom wavefunction. Exactly the same interference pattern as is shown for light fields in chapter 3 can thus be created in a Bose-Einstein Condensate. Amongst other things it was possible to stimulate a vortex pair with opposite circulation direction, which was also identified by interferometry.

6.1 Observation of Raman transitions

Before projecting light beams with angular momentum, the Raman setup was tested. This section presents some quantitative results taken at different stages of the experiment.

All experiments started out with a ${}^{87}Rb$ Bose-Einstein Condensate of approximately 3.5 million atoms in the $|5^2S_{1/2}; F = 1\ m_F = -1\rangle$ state. The total number of atoms was calculated from equation 5.4. $14ms$ after being released from the trap (time of flight), both copropagating Raman beams were switched on for a defined amount of time. Thus a fraction of the atoms was transfered to the $|5^2S_{1/2}; F = 2\ m_F = 1\rangle$ state by driving transitions with σ^+- and σ^--polarized light fields as shown in figure 4.9. Figure 6.1 shows a Rabi oscillation of the system. The data was fitted with

$$f(t) = A + \frac{1}{2}B\Big(1 - \cos(wt - t_0)e^{-t/\tau}\Big) \tag{6.1}$$

where A, B, w, t_0, τ are fit parameters. Formula 6.1 takes an exponential damping with the characteristic time τ, a phase offset t_0 and an amplitude different from 1 into

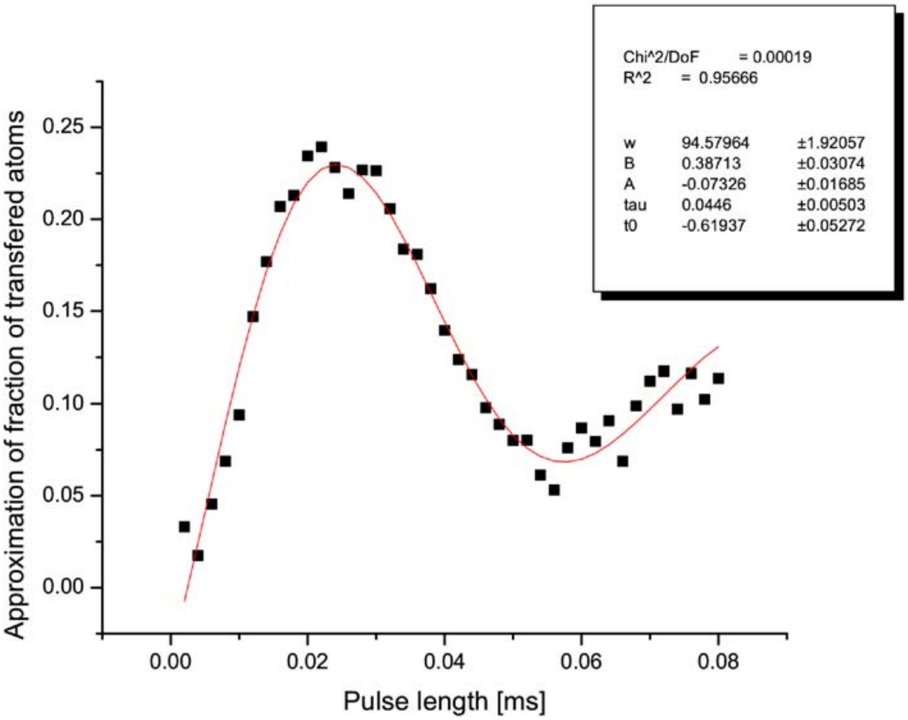

Figure 6.1: Transfered fraction of the atoms as a function of the pulse length. The intensites of both Raman beams were set to $6\mu W/\pi(75\mu m)^2$, a detuning of $\Delta_{lock} = 2\pi \cdot 5.2GHz$ and a 2 photon detuning of $\delta = 2\pi \cdot 5KHz$ was chosen.

account. The values obtained for the respective parameters are shown in the figure. To calculate an approximate Rabi frequency for this 4 level system, the transfer rates via the two intermediate states $|5^2P_{1/2}; F = (1, 2)\ m_F = 0\rangle$ were added. Using equation 4.10 to calculate the expected pulse length for maximum transfer (π-pulse) in this way gives $10\mu s$, which is roughly in agreement with the experimental data. Clearly, there is a strong damping mechanism visible in this dataset. A detuning of $\Delta_{lock} = 2\pi \cdot 5.2GHz$ corresponds to a detuning $\Delta = 2\pi \cdot 800MHz$ of the shifted light field from the upper intermediate level. Looking at figure 4.11, it can be seen that the expected spontaneous scattering rate for this detuning during a $60\mu s$ pulse is around 18%, which may explain the damping.

Only 34% of the light in the EOM beam is in the first order and also the Clebsch-Gordan coefficient for the σ^+ transition is smaller by a factor of 3. The differential Stark shift due to this is approximated with equation 4.7 to be $\delta^{AC}_{F'=2} = 164kHz$ for the upper level and $\delta^{AC}_{F'=1} = 80kHz$ for the lower level. If not compensated, this leads to a two photon detuning, which limits the maximum transfer. From equation 4.10 the maximum expected transfer by transitions via the respective levels is computed

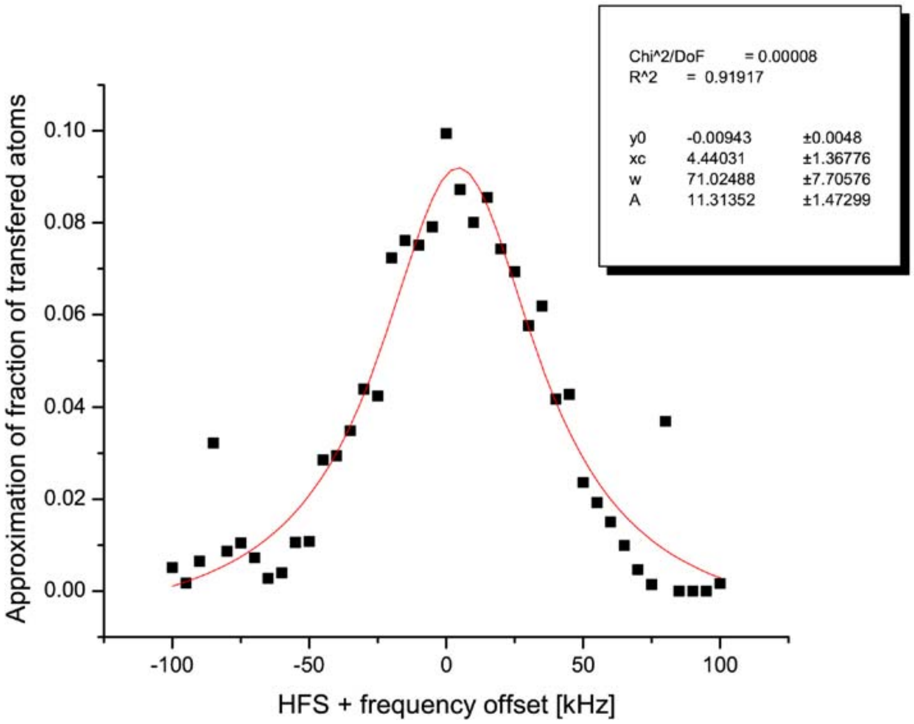

Figure 6.2: Transfer as a function of the two photon detuning. The Raman pulse duration for this dataset was $12\mu s$.

to be

$$\frac{|^{(F'=1,2)}\Omega_{eff}|^2}{^{(F'=1,2)}\Omega_r^2} \approx 0.35 \tag{6.2}$$

slightly higher than the measured one, which is only approximate however. This might be due to the damping.

For graph 6.2 the two photon detuning was scanned by changing the modulation frequency of the EOM. A Lorentzian was fitted to this dataset. The Stark shift offset might be too small to be evident in this graph since it is only $\delta f^{AC}_{F'=2} = 26kHz$ and $\delta f^{AC}_{F'=1} = 12kHz$ for respective levels and the line is clearly broadened. The maximum transfer in this graph may then be limited by the pulse length. Since very small beam cross sections were used to collect both datasets, it might be that not both beams were hitting the atom cloud centered and overlapping well. This could have led to a much bigger differential Stark shift than assumed in equation 6.2 and, if the intensity of one of the beams at the location of the cloud was significantly smaller, also to slower Rabi cycling. A hint towards this might also be the line broadening since, if different sections of the cloud would have seen different beam intensities and thus the Rabi frequencies and the Stark shifts might have been locally different, one would expect a broader line. The line broadening cannot be totally due to the short pulse

that was applied. Was it merely due to the pulse duration one would expect it to be $\Delta f = 1/2\pi 12\mu s \approx 13.3kHz$ for the $12\mu s$ pulse.
The transfer efficiency was not optimized, since high transfer rates were not wanted in the vortex experiments. This is because we did not want to detune the imaging light to avoid the refractive effects mentioned in 5.2 of the Bose-Einstein Condensate itsself. For the use with fewer atoms in the surface trap, the efficiency will however need to be improved. For that, a detailed calculation of the differential Stark shifts caused by all light fields might be needed.
Another limitation for the transfer rates in the experiments might be due to the experimental sequence. It cloud be that during trap shut-off and time of flight expansion, other Zeeman states get populated, which don't get transfered by the Raman pulses, leading to lower transfer when compared to the total number of atoms.

6.2 Results of vortex projection

This section presents the images taken of the cloud after projecting a hologram. Two holograms that were projected: The first one contained a single vortex in the region were the Gaussian beam that illuminated it was not negligible. A second one contained a structure for two counterpropagating vortices. Vortices were induced in the cloud by driving hyperfine state changing Raman transitions as before, but now one of the light beams was carrying orbital angular momentum.
By applying a second Raman pulse with the two Gaussian beams, it was possible to interfere the Bose-Einstein Condensate in the vortex state with a constant phase one. The pulse sequence makes it clear that the phase of the classical electrical field was indeed stored in the atom wavefunctions, since the beams of the Raman setup that have a stationary interference pattern were not switched on at the same time. The whole sequence for the interference experiments is summarized in the table. For the

Sequence for interferometry experiments		
Time	Action	Effect
$t = 0$	Trap shutoff	Start of time of flight
$t = 14ms$	First Raman pulse. Vortex beam + EOM Gaussian beam are applied	Fraction of atoms transfered into a vortex state
$t = 14ms$ + first Raman pulse length	Second Raman pulse. Plain Gaussian + EOM Gaussian Beam are applied	Interference between both states
$t = 17ms$	$F = 2 \rightarrow F' = 3$ imaging light applied	Absorption imaging

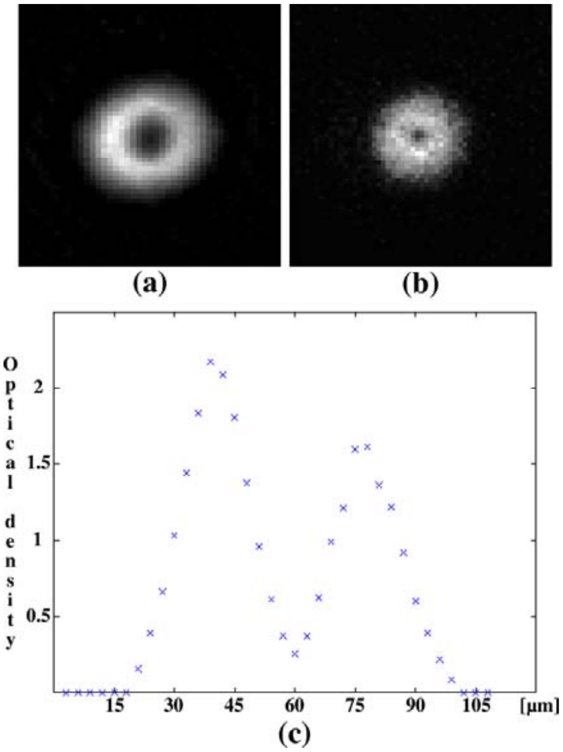

Figure 6.3: (a),(b) absorption images of single vortex states. Imaging magnification was 6.6, which means one pixel, which is $20\mu m$ in our camera, corresponds to $\sim 3\mu m$ in the cloud. (a) telescope magnification was set to: projection 0.15. (b) telescope magnification: projection 0.075. (c) optical density profile on path straight through the vortex core of image (a).

images of solely the vortex state, the second Raman pulse was not applied.
Since the projection and imaging system consists of a simple arrangement of achromatic lenses, the resolution of both were limiting for the experiments. Thus we did not project the vortex beams onto the cloud while still in trap, but after $14ms$ time of flight, when it had expanded by roughly a factor of two. An absoption image of the cloud was taken $3ms$ after applying the Raman pulses.
It will be interesting to proceed with the experiments once the final high resolution objective is installed. Then it will become possible to study the stability of vortices and the dynamics of the condensate containing vortices with in trap experiments.

6.2.1 Single vortex

Figure 6.3 shows two absorption images of condensate states carrying one quantum of angular momentum. The Raman pulse durations were (a) $4\mu s$ and (b) $6\mu s$. Intensities and detunings were chosen to be: (a) $\Delta_{lock} = 5.2GHz$, $6.2\mu W/\pi(75\mu m)^2$ and (b) $\Delta_{lock} = 1.8GHz$, $10\mu/\pi(131\mu m)^2 W$, where the radii in the denominators are for the beam after demagnification.

Both pictures result from projecting a slightly defocused vortex, where in image (a) the defocusing was stronger. This is why the core looks bigger. From figure 3.13 it can be seen that if the image plane is not in the plane of the atom cloud, the size of the vortex core in the light beam is bigger. This means that also in the condensate cloud, the region where the atoms have not undergone a Raman transition is bigger. For our case this was wanted, since the imaging resolution was otherwise not enough to see the vortex core. A depth of focus calculation for the projection system used in (a) showed that the vortex core in the beam roughly doubles its size for a displacement $d = 200\mu m$ from the image plane. That the effect of differently well focused projection can be seen in the images of the cloud shows that the condensate had not equilibrated after $3ms$ more time of flight. Equilibration is expected to be slow after $14ms$ time of flight, since it depends on the interactions, which are already small after this expansion time.

Figure 6.4 shows 4 pictures for which the vortex state was interfered with a constant phase one. For that, two Raman pulses of $4\mu s$ duration were applied directly after one another. The other parameters were the same as for figure 6.3(a). The phases between the vortex beam and the Gaussian EOM beam were different for each of the pictures. Thus the regions of constructive/destructive interference can be seen in different locations. The picture resembles the one in figure 3.9, which was taken with a Mach-Zehnder interferometer for light (see chapter 3).

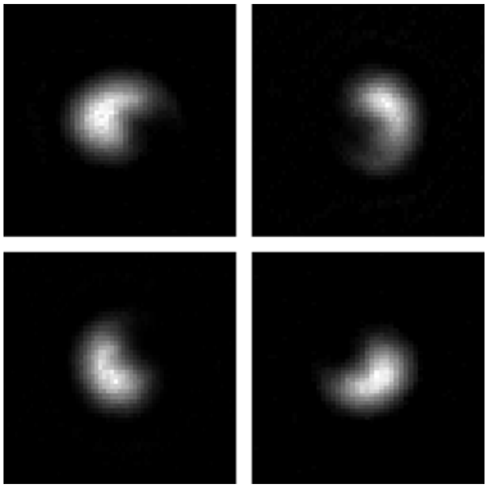

Figure 6.4: Interference of a single vortex state with a plane phase.

If the plain Gaussian beam (reference beam) that is used together with the EOM

Gaussian beam in the second pulse for the interference pulse sequence is not exactly copropagating with the vortex beam, an interference pattern that resembles the hologram pattern itsself can be produced. A cloud that is interfering in this way is shown in figure 6.5(a),(b). Like in all the experiments presented, the interference of the Bose-Einstein Condensate is just the same as in the light beams. Thus the interference pattern is the same as was calculated in chapter 3, equation 3.8, where there is an angle θ between the object beam and the reference beam. Figure 6.5(c) shows a picture with a tilted reference beam which was also taken with the Mach-Zehnder interferometer for light.

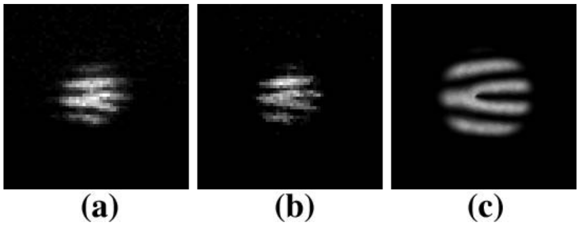

Figure 6.5: (a), (b) interference with a reference beam that is not copropagating. Intensity, detuning and beam radii were $\Delta_{lock} = 1.8GHz$, $10\mu/\pi(131\mu m)^2W$ for these experiments. (c) interference of a light beam containing a single vortex with a tilted reference beam.

However, it needs to be emphasized again that this resemblance is due to the wave nature of matter. It is not the case that the plain Gaussian beam is interfering with the vortex beam, thus transfering atoms only where there is constructive interference between both beams. Rather, the wavefunctions, which obtained their phase from the classical electromagnetic field during the Raman transitions, of the vortex state and the state with plane phase interfere and this inteference pattern is recorded. The fact that these two beams are not switched on at the same time makes this clear.

6.2.2 Counter spinning vortex pair

We succeeded in exciting a state with two counter spinning vortices by projecting the corresponding hologram. Two images of clouds in this state are shown in figure 6.6. In the hologram, the fork like structures (pointing towards each other for counterpropagating vortices) where spaced by $330\mu m$, which demagnified by a factor of 0.075 resulted in a spacing of $24.75\mu m$ in the image plane. As before, both images result from projecting a slightly defocused vortex pair, which was done for better visibility (or better, visibility at all) of the vortex cores.

Figure 6.7 shows results from a depth of focus calculation for two vortices, which was described in 3.2.4. The numerical aperture of $NA = 0.16$ corresponds to the projection system that demagnifies by a factor of 0.075. The shown patterns are best case,

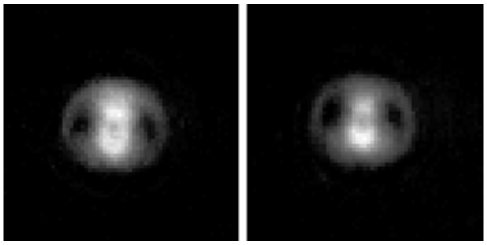

Figure 6.6: Counter spinning vortices. Experimental parameters were $\Delta_{lock} = 1.8GHz$, $10\mu/\pi(131\mu m)^2W$ and pulse duration $8\mu s$.

since a diffraction limited system was assumed. Aberations and some dust resulted in a worse intensity profile. It can be seen, that the vortex core size in the beams rapidly grows bigger from the image plane to a plane that is displaced by $d = 100\mu m$. At around $d = 200\mu m$ the diffraction rings around the vortex cores can be seen to overlap in the region between the cores. This leads to higher intensity in this region. For larger displacements, the cores change shape.

Looking again at picture 6.6, it can be seen that the Raman transfer rate between the vortex centers was much higher than on the outside. In between the vortex cores the atoms were even transfered back, which means the pulse duration for this region correspondend to more than a π-pulse. The high transfer rates in between the cores is probably an artifact of defocusing. Comparing figures 6.7 and 6.6, one can estimate that displacement of the image plane in the experiment was around 200-300μm. During the experiments the focusing of the projection was often changed. For focusing, a lens of the telescope arrangement was moved on a rail system. Starting on one (defocused) side, the vortex cores in the atom clouds could be seen to grow smaller, disappear and the reappear, as expected from figure 6.7.

Interference experiments were also performed with the counter spinning vortex pair.

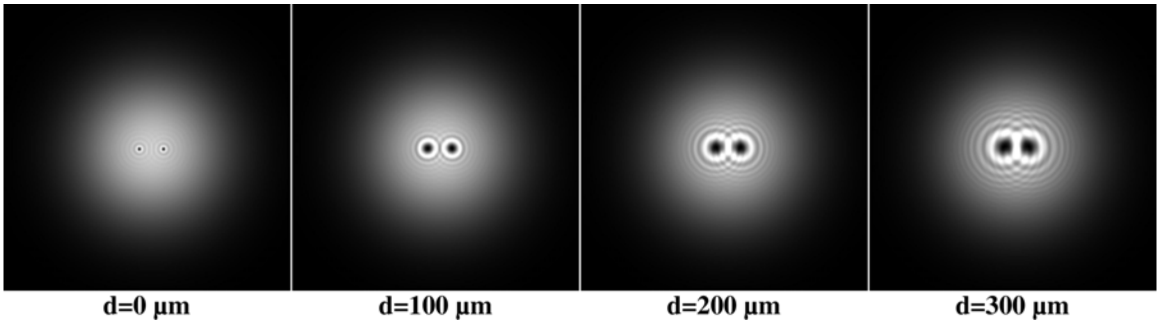

Figure 6.7: Change in the intensity pattern for defocused projection. The calculation was done for a diffraction limited projection system of $NA = 0.16$.

The results are shown in the last figure in this chapter. Two $4\mu s$ pulses were applied; the other parameters were $\Delta_{lock} = 1.8GHz$, $10\mu/\pi(131\mu m)^2W$. The column (a) shows absorption images of the cloud for different relative phases between the vortex state and the reference beam. Calculated interference pattern for a counter spinning vortex pair (b) and a copropagating vortex pair (c) can be compared to the pictures in column (a). The relative phases for the calculations that approximately resemble the ones seen (a), are given on the right. From this, the vortex pair can definitely be identified as a counter rotating one.

Figure 6.8: (Back of the page) Interference of the counter spinning vortex pair with a plane phase reference state. Column (a) shows the interference pattern for different relative phases of both states. For comparison, calculated interference patterns for a counter spinning vortices (b) and co-spinning vortices are shown. The vortex pair can clearly be identified as counter spinning.

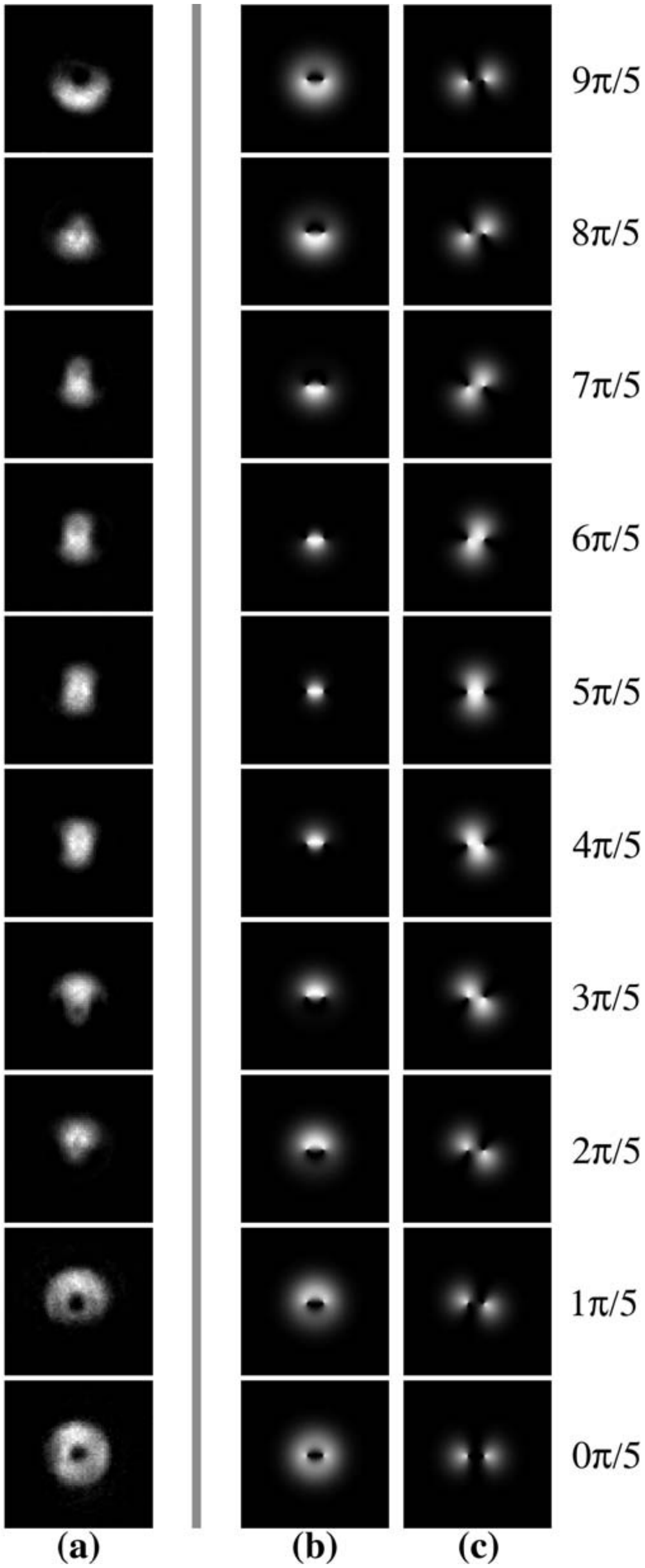
9π/5
8π/5
7π/5
6π/5
5π/5
4π/5
3π/5
2π/5
1π/5
0π/5
(a)
(b)
(c)

Conclusion

The work described in this thesis successfully demonstrates the scheme of inducing vortices in a cloud of ultracold atoms by transfer of orbital angular momentum quanta from light beams. By exploitation of the coherence property of Raman transitions it was possible to prepare defined internal and momentum states of atoms in a Bose-Einstein Condensate.

The results in chapter 6 show that the usefulness and versatility of this scheme relies critically on the resolution with which the orbital angular momentum beams are projected. In the presented experiments, it was only possible to project two vortices onto the Bose-Einstein Condensate during time of flight due to this limitation. Also since the observed core size depended rather on projection than on the Bose-Einstein Condensate itself, no information about the structure of the vortex could be gained. However, the stimulation of a state with counter propagating vortices is notable since this is not easily possible with common stirring techniques.

There are many interesting questions for the experiments to follow. In the introduction, it is mentioned that low filling factors of vortices are an interesting regime for research. In principle, the resolution of the chrome mask holograms is high enough to have many vortex structures on an area that is still usable. It is described in chapter 3 how to make holograms with many vortices. With the final imaging system, it should be possible to project a low filling factor regime. It will be interesting to find out, if any useful information can be obtained from a non equlibrium situation created in this way.

Interesting are, of course, experiments with the cloud still in trap. Only like this is it possible to study the stability and dynamics of vortex states for longer periods without parameters, such as density, changing. The influence of interactions will be interesting to observe.

Vortices were induced by Raman transitions with copropagating beams that changed the hyperfine and magnetic state. Thus, although in the absorption images not visible, the other spin state is still present in the cloud. Structures with spin textures as the one created in our experiment have raised the interest of researchers since the 1960s and are referred to as skyrmions (called after T. H. R. Skyrme) or merons [52, 53, 54].

The interaction of the atoms of the same spin state and those in the other spin state is different. It will be interesting to see the effect of this difference in interaction on parameters like vortex core size or vortex dynamics in the condensate. Since the intensity in the vortex core of the *light beam* is very low, the atoms there do not take part in the Raman transition. This means, that the vortex core is filled with atoms of the other spin state interacting with the atoms in the vortex state. By improving the transfer efficiency, it will then be possible to produce a vortex states where only in the cores there are still atoms of the other spin state. Thus, for those experiments, the relevant quantity for the behaviour of the wavefunction, close to the vortex core, may be the spin healing length and not the healing length introduced in section 2.3.1.

Bibliography

[1] E. L. Raab, M. Prentiss, A. Cable, S. Chu, and D. E. Pritchard, "Trapping of Neutral Sodium Atoms with Radiation Pressure," *Phys. Rev. Lett.* **59** (Dec, 1987) 2631–2634.

[2] M. Anderson, J. Ensher, and E. A. Cornell, "Observation of Bose-Einstein Condensation in a Dilute Atomic Vapor," *Science* (1995).

[3] C. C. Bradley, C. A. Sackett, J. J. Tollett, and R. G. Hulet, "Evidence of Bose-Einstein Condensation in an Atomic Gas with Attractive Interactions," *Physical Review Letters* (1995).

[4] K. B. Davis, M. O. Mewes, M. R. Andrews, N. J. van Druten, D. S. Durfee, D. M. Kurn, and W. Ketterle, "Bose-Einstein Condensation in a Gas of Sodium Atoms," *Physical Review Letters* (1995).

[5] R. P. Feynman, "Simulating physics with computers," *International Journal of Theoretical Physics* (1982), no. 21,.

[6] R. P. Feynman, "Tiny Computers Obeying Quantum Mechanical Laws," in *New Directions in Physics: The Los Alamos 40th Anniversary Volume*, D. M. K. N. Metropolis and G.-C. Rota, eds. Academic Press, Inc.

[7] S. LLoyd, "Universal Quantum Simulators," *Science* **273** (1996) 1073.

[8] M. Greiner, O. Mandel, T. Esslinger, T. W. Hänsch, and I. Bloch, "Quantum Phase Transition from a superfluid to a Mott insulator in a gas of ultracold atoms," *Nature* **415** (2002).

[9] S. Inouye, M. R. Andrews, J. Stenger, H.-J. Miesner, D. M. S. Kurn, and W. Ketterle, "Observation of Feshbach resonances in a Bose-Einstein condensate," *Nature* (1998).

[10] G. Thalhammer, K. Winkler, F. Lang, S. Schmid, R. Grimm, and J. H. Denschlag, "Long-Lived Feshbach Molecules in a Three-Dimensional Optical Lattice," *Physical Review Letters* **96** (2006), no. 5, 050402.

[11] L. Santos, M. A. Baranov, J. I. Cirac, H.-U. Everts, H. Fehrmann, and M. Lewenstein, “Atomic Quantum Gases in Kagomé Lattices,” *Physical Review Letters* **93** (2004), no. 3, 030601.

[12] M. Greiner, I. Bloch, T. W. Hänsch, and T. Esslinger, “Magnetic transport of trapped cold atoms over a large distance,” *Physical Review A* **63** (2001).

[13] M. R. Andrews, W. Ketterle, *et al.*, “Observation of Interference Between Two Bose Condensates,” *Science* (1997).

[14] M. W. Zwierlein, C. A. Stan, C. H. Schunck, S. M. F. Raupach, S. Gupta, Z. Hadzibabic, and W. Ketterle, “Observation of Bose-Einstein Condensation of Molecules,” *Physical Review Letters* (2003).

[15] C. A. Regal, M. Greiner, and D. S. Jin, “Observation of Resonance Condensation of Fermionic Atom Pairs,” *Physical Review Letters* (2004).

[16] J. R. Abo-Shaeer, W. Ketterle, *et al.*, “Observation of Vortex Lattices in Bose-Einstein Condensates,” *Science* (2001).

[17] E. M. Lifshitz, *Statisical Mechanics.* Butterworth Heinemann, 1980.

[18] R. J. Donnelly, *Quantized Vortices in Helium II.* Cambridge University Press, 1991.

[19] K. Huang, *Statistical Mechanics.* Wiley, second ed., 1987.

[20] D. S. Petrov, M. Holzmann, and G. V. Shlyapnikov, “Bose-Einstein Condensation in Quasi-2D Trapped Gases,” *Phys. Rev. Lett.* **84** (Mar, 2000) 2551–2555.

[21] Z. Hadzibabic, P. Krüger, M. Cheneau, B. Battelier, and J. Dalibard, “The atomic Bose gas in Flatland,” *arXiv:cond-mat/0609761v1* (2006).

[22] G. Baym, “Tkachenko Modes of Vortex Lattices in Rapidly Rotating Bose-Einstein Condensates,” *Phys. Rev. Lett.* **91** (Sep, 2003) 110402.

[23] N. R. Cooper, N. K. Wilkin, and J. M. F. Gunn, “Quantum Phases of Vortices in Rotating Bose-Einstein Condensates,” *Phys. Rev. Lett.* **87** (Aug, 2001) 120405.

[24] B. Paredes, P. Fedichev, J. I. Cirac, and P. Zoller, “$\frac{1}{2}$-Anyons in Small Atomic Bose-Einstein Condensates,” *Phys. Rev. Lett.* **87** (Jun, 2001) 010402.

[25] V. Schweikhard, I. Coddington, P. Engels, V. P. Mogendorff, and E. A. Cornell, "Rapidly Rotating Bose-Einstein Condensates in and near the Lowest Landau Level," *Physical Review Letters* **92** (2004), no. 4, 040404.

[26] E. Cage, R. F. Dziuba, and B. F. Field, "Quantum Hall Effect in a GaAs/AlGaAs Heterostructure," *IEEE Trans. Instrum. Meas.* **IM-34** (1985).

[27] P. C. Haljan, I. Coddington, P. Engels, and E. A. Cornell *Phys. Rev. Lett.* **87** (Nov, 2001) 210403.

[28] B. E. A. Saleh and M. Teich, *Fundamentals of Photonics.* Wiley, 1991.

[29] M. Hafezi, A. Sørensen, E. Demler, and M. Lukin, "Fractional Quantum Hall Effect in Optical Lattices," *APS Meeting Abstracts* (May, 2006) G1073+.

[30] A. Einstein, *Quantentheorie des einatomigen idealen Gases.* Walter de Gruyter u. Co., 1925.

[31] H. S. C. J. Pethick, *Bose-Einstein Condensation in Dilute Gases.* Cambridge University Press, 2002.

[32] C. Raman, J. R. Abo-Shaeer, J. M. Vogels, K. Xu, and W. Ketterle, "Vortex Nucleation in a Stirred Bose-Einstein Condensate," *Phys. Rev. Lett.* **87** (Nov, 2001) 210402.

[33] E. Lundh, C. J. Pethick, and H. Smith, "Zero-temperature properties of a trapped Bose-condensed gas: Beyond the Thomas-Fermi approximation," *Phys. Rev. A* **55** (Mar, 1997) 2126–2131.

[34] E. Lundh, C. J. Pethick, and H. Smith, "Vortices in Bose-Einstein-condensed atomic clouds," *Phys. Rev. A* **58** (Dec, 1998) 4816–4823.

[35] S. J. van Enk *et al.*, "Spin and Orbital Angular Momentum of Photons," *Europhys. Lett.* **25** (1994) 497–501.

[36] Allen *et al.*, "Orbital Angular Momentum of light and the transformation of Laguerre-Gaussian Laser Modes," *Physical Review A* **45** (1992), no. 11,.

[37] H. M. Smith, *Principles of Holography.* Wiley, second ed., 1969.

[38] E. Hecht, *Optics.* Addison Wesley, fourth ed., 2002.

[39] P. Berman, ed., *Atom Interferometry.* Academic Press, 1997.

[40] J. J. Sakurai, *Modern Quantum Mechanics.* Addison Wesley Longman, revised ed., 1994.

[41] M. Lukin, “Atomic Molecular Optics 2.” Lecture Notes.

[42] M. O. Scully and M. S. Zubairy, *Quantum Optics*. Cambridge University Press, 1997.

[43] R. Grimm and M. Weidemüller, “Optical dipole traps for neutral atoms,” *Advances in Atomic, Molecular and Optical Physics* (1999).

[44] M. Greiner, *Ultracold quantum gases in three-dimensional optical lattice potentials*. PhD thesis, Ludwig-Maximilians Universität München.

[45] K. Bergmann, H. Theuer, and B. W. Shore, “Coherent population transfer among quantum states of atoms and molecules,” *Rev. Mod. Phys.* **70** (Jul, 1998) 1003–1025.

[46] J. Stenger, S. Inouye, A. P. Chikkatur, D. M. Stamper-Kurn, D. E. Pritchard, and W. Ketterle, “Bragg Spectroscopy of a Bose-Einstein Condensate,” *Phys. Rev. Lett.* **82** (Jun, 1999) 4569–4573.

[47] D. A. Steck, “Rubidium 87 D Line Data,” tech. rep., Los Alamos National Laboratory, 2001.

[48] W. Demtröder, *Laser Spectroscopy*. Springer, third ed., 2003.

[49] G. C. Bjorklund, “Frequency-modulation spectroscopy: a new method for measuring weak absorptions and dispersions,” *Optics Letters* (1980).

[50] R. Harjani and L. Dai, *Design of Higher-Performance CMOS Voltage Controlled Oscillators*. Springer, 2003.

[51] M. R. Matthews, *Two Component Bose-Einstein Condensation*. PhD thesis, University of Texas, 1994.

[52] A. E. Leanhardt, Y. Shin, D. Kielpinski, D. E. Pritchard, and W. Ketterle, “Coreless Vortex Formation in a Spinor Bose-Einstein Condensate,” *Phys. Rev. Lett.* **90** (Apr, 2003) 140403.

[53] N. D. Mermin and T.-L. Ho, “Circulation and Angular Momentum in the A Phase of Superfluid Helium-3,” *Physical Review Letters* **36** (1976).

[54] P. W. Anderson and G. Toulouse, “Phase Slippage without Vortex Cores: Vortex Textures in Superfluid ^3He,” *Physical Review Letters* (1977).

Acknowledgement

First of all I would like to thank the whole group for the good atmosphere and support throughout this whole year. It was great working with you and I learned a lot.

Especially I would like to thank Markus Greiner for the extraordinary good mentoring. In fact, I cannot imagine what could have been better. A good mentoring of diploma thesis is not self-evident, as I know from a lot of friends. So I am very thankful for that.

Without the agreement of Prof. T. Hänsch to support this external diploma thesis for the Ludwig-Maximillians Universität München, all this would not have been possible. I thank him for giving me the chance of going abroad as I wanted to.

Were it not for Waseem Bakr, there would propably not have been the results that I was able to present in this thesis. I admire the expertise with which he solved a lot of problems. Also, I thank him for the driving force in some of the long nights towards the end of this thesis . . .

I thank Amy Peng for the discussions and her competent answering of all my questions. Usually the answers were exactly what I needed to hear to understand the subject. I like her way of explaining physics and the way she thinks about it.

I thank Jon Gillen for the expertise with which he helped me building things for this experiment. I had a fun time with him and he is an awesome labmate.

In this place I would like to thank my parents for supporting me in every respect during the whole of my study. Without this, it would propably not have been possible for me to get this far in studying physics which I love so much.

I would also like to thank my girlfriend Natalia Garcia for her support while I was abroad. It made it a lot easier that she came to visit me for such a long time and I thank her for her patience.

Erklärung

Hiermit erkläre ich, dass ich die Arbeit selbständig verfasst und keine anderen als die angegebenen Quellen und Hilfsmittel benutzt habe.

Datum	Unterschrift